



Deposited via The University of Leeds.

White Rose Research Online URL for this paper:

<https://eprints.whiterose.ac.uk/id/eprint/175861/>

Version: Accepted Version

---

**Article:**

Lloyd, GE, Lee, AL and Kahl, M (2021) A practical method to determine the five-parameter orientation of intragranular boundaries in polycrystals. *Tectonophysics*, 814. 228955. ISSN: 0040-1951

<https://doi.org/10.1016/j.tecto.2021.228955>

---

© 2021, Elsevier. This manuscript version is made available under the CC-BY-NC-ND 4.0 license <http://creativecommons.org/licenses/by-nc-nd/4.0/>.

**Reuse**

This article is distributed under the terms of the Creative Commons Attribution-NonCommercial-NoDerivs (CC BY-NC-ND) licence. This licence only allows you to download this work and share it with others as long as you credit the authors, but you can't change the article in any way or use it commercially. More information and the full terms of the licence here: <https://creativecommons.org/licenses/>

**Takedown**

If you consider content in White Rose Research Online to be in breach of UK law, please notify us by emailing [eprints@whiterose.ac.uk](mailto:eprints@whiterose.ac.uk) including the URL of the record and the reason for the withdrawal request.



9 **Abstract-**Intragranular boundaries are important features of polycrystalline materials and impact on  
10 many physical and chemical properties. Knowledge of their physical orientation is often crucial to  
11 explain such properties. However, it has proved difficult to determine the complete orientation of  
12 intragranular boundaries, which involves the misorientation angle and axis about which the adjacent  
13 crystal lattices need to be rotated to bring them into coincidence and also the physical orientation of  
14 the boundary plane, expressed by the plunge and azimuth of its normal; five parameters in total.  
15 Here we present a simple and practical manual method to determine the complete intragranular  
16 boundary orientation in any crystal system. The method is developed on geometrical relationships  
17 exhibited between electron channelling patterns across a common boundary but then extended for  
18 use with electron backscattered diffraction patterns. The method recognises the  
19 channelling/diffraction band, equivalent to a crystal lattice plane, not displaced across a boundary;  
20 the boundary rotation axis must be the normal to this plane. Geometrical relationships between the  
21 boundary trace, the non-displaced band/plane and their respective plane normals constrain boundary  
22 orientation to two alternative symmetrically equivalent solutions and are evaluated via  
23 stereographic projection. The choice of solution is guided by comparison with the presence or  
24 absence of a similarly oriented band/plane observed in the original channelling/diffraction patterns.  
25 The method therefore conforms to the low-index crystallographic lattice plane and dislocation  
26 model for intragranular boundary formation and defines boundary orientation in terms of total  
27 angular misorientation due to tilt and twist components and the orientation of the boundary plane.  
28 Examples of intragranular boundary orientation determination using this method are provided in  
29 olivine. Results are compared to and differ from those obtained via conventional misorientation  
30 analysis, which only rotates adjacent crystal lattices into parallelism and does not consider boundary  
31 plane orientation. Potential extrapolation of the new method to intergranular boundaries is also  
32 considered.

## 1. INTRODUCTION

33

34 Intragranular boundaries are important and common features of polycrystalline materials, such as  
 35 metals, ceramics and rocks. Their presence impacts critically on many physical and chemical  
 36 properties, processes and behaviours, including: overall strength and failure, various types of  
 37 conductivity, diffusion and creep mechanisms, recrystallisation and recovery processes, corrosion  
 38 and precipitation behaviours, etc (e.g. Randle, 1993). Thus, the nature of intragranular boundaries is  
 39 crucial to understanding the ultimate behaviour of polycrystalline materials. However, intragranular  
 40 boundaries often exist as rather obscure elements within more detailed microstructural  
 41 characterisations that focus on the properties of the regions they surround, such as the crystal  
 42 texture or fabric (as defined by the crystallographic preferred orientation or CPO), subgrain size,  
 43 etc. Perhaps the main reason why intragranular boundaries are often somewhat neglected is due to  
 44 problems associated with defining their complete physical and/or crystallographic orientations.

45 On the one hand, intragranular boundaries are defects that perturb the crystallographic structure of  
 46 polycrystalline materials; their definition must include recognition of this impact on the  
 47 crystallography. Convention therefore recognises the misorientation angle/axis ( $\theta/\langle uvw \rangle$ ) pair, or  
 48 the crystallographic direction about which one crystal lattice must be rotated by a (minimum) angle  
 49 to bring it into coincidence with an adjacent lattice. As this operation represents a pure rotation of  
 50 one crystal coordinate system with respect to the other (Fig. 1a), it can be described by a rotation  
 51 transformation matrix ( $g_m$ ), such that,

$$52 \quad \{C_i\} = g_m \{C_j\} \quad (1)$$

53 where  $\{C_i\}$  and  $\{C_j\}$  are the respective adjacent crystal coordinate systems. Misorientation  
 54 angle/axis pairs comprise three degrees of freedom: the plunge/azimuth of the axis and the angle  
 55 (e.g. Warrington and Bufalini, 1971; Grimmer et al., 1974; Mainprice et al., 1993; Lloyd et al.,  
 56 1997; Randle, 2003). On the other hand, intragranular boundaries are also physical features (i.e.  
 57 ‘planes’), the orientation of which is typically crystallographically constrained but is not necessarily

58 crystallographically coincident. The physical orientation of the intragranular boundary plane is  
 59 defined by the plunge/azimuth of the normal to the plane, which involves two degrees of freedom  
 60 (Fig. 1b); however, it can also be represented crystallographically (i.e.  $\langle uvw \rangle$ ) with respect to one  
 61 and/or other of the two adjacent crystal orientations.

62 Thus, the complete orientation of intragranular boundaries involves five independent parameters  
 63 (e.g. Sutton and Balluffi, 1995; Kim et al., 2005; Randle, 2006; Rohrer and Randle, 2009;  
 64 Ratanaphan et al., 2014; Sutton et al., 2015; Dash et al., 2017). However, whilst it is always  
 65 possible to determine the misorientation angle/axis pair, particularly via electron backscattered

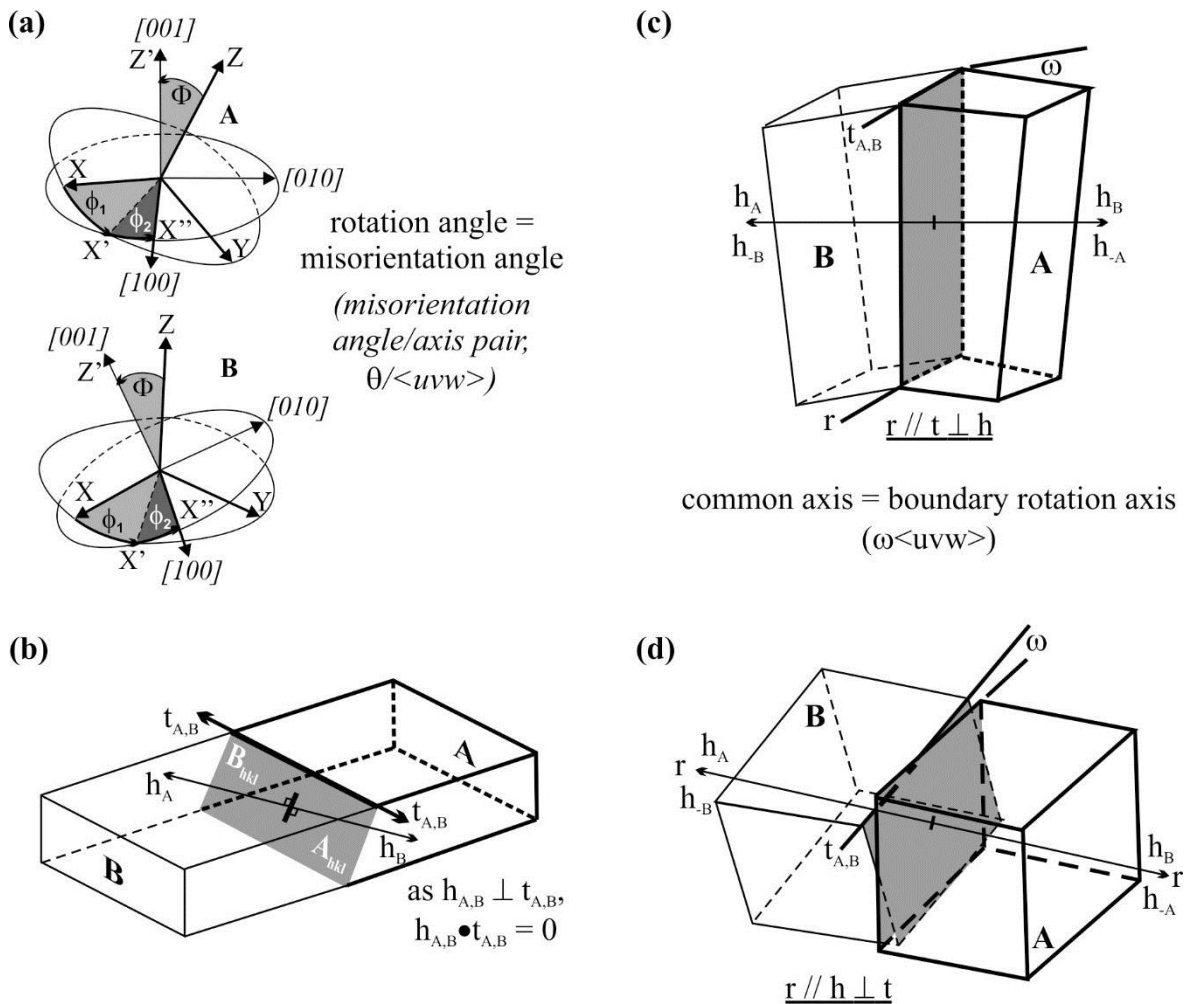


**Figure 1.** Intragranular boundary relationships. (a) Definition of the crystallographic orientations of two subgrains A and B and the alternative three rotations ( $\phi_1$ ,  $\Psi$ ,  $\phi_2$ ) required to bring their respective lattices XYZ and X'Y'Z' into coincidence, as represented by the misorientation angle/axis pair. (b) Regions A, B share common boundary plane ( $A_{hkl}$ ,  $B_{hkl}$ ), trace (t) and normal (h). (c) Pure tilt boundary (r, rotation axis;  $\omega$ , rotation angle). (d) Pure twist boundary.

66 diffraction (EBSD) in the scanning electron microscope (SEM), the direction of the boundary plane  
67 normal has proved to be notoriously difficult to establish. Although various methods, techniques  
68 and approaches do exist (e.g. optical microscopy universal stage, transmission electron microscopy,  
69 focussed ion beam, X-ray and neutron techniques, etc.), they tend to be restrictive, laborious,  
70 complex and/or expensive (e.g. Rohrer & Randle, 2009). An exception to these constraints is  
71 provided by the grain boundary character distribution (GBCD) method (e.g. Saylor et al., 2004;  
72 Rohrer et al., 2004b), which combines EBSD misorientation analysis and statistical stereology of  
73 boundary traces. However, GBCD has been reserved mostly for (cubic) metals and ceramics (e.g.  
74 Saylor et al. 2004), with only a single geological application on olivine (Marquardt et al., 2015).

75 More general characterisation of boundary microstructural data has recently become more common  
76 using SEM/EBSD. In part, this stems from the availability of free resource software. Perhaps the  
77 most readily available is *MTEX* (e.g. Bachmann et al., 2010) and in particular its *Tilt and Twist*  
78 *Boundaries* script (<https://mtex-toolbox.github.io/TiltAndTwistBoundaries.html>). Analytical scripts  
79 based on the GBCD method for estimating the five grain boundary parameters are also available  
80 ([http://mimp.materials.cmu.edu/~gr20/Grain\\_Boundary\\_Data\\_Archive/](http://mimp.materials.cmu.edu/~gr20/Grain_Boundary_Data_Archive/)). In addition, an alternative  
81 but related approach using the weighted mean Burger's vector has been suggested by Wheeler et al.  
82 (2009), with a recent modification within the MTEX software package (Wieser et al., 2020).

83 However, all approaches are based a priori on the recognition of tilt and twist boundaries based on  
84 accurate definition of the misorientation axis; they do not consider either general boundaries or the  
85 orientation of the boundary plane normal. Thus, they recognise only three of the five parameters  
86 necessary to fully define an intragranular boundary.

87 The physical orientation of the boundary between two intragranular domains (A, B) can be  
88 described crystallographically relative to either domain (i.e.  $A_{hkl}$ ,  $B_{hkl}$ ; see Fig. 1b). The boundary  
89 plane can also be described by its trace ( $t_{A=B}$ ) and normals ( $h_{A,B}$ ) relative to either grain. As these  
90 are perpendicular,

$$91 \quad h_{A,B} \cdot t_{A,B} = 0 \quad (2)$$

92 Within this construction, two ideal ‘end-member’ intragranular boundary configurations can be  
93 recognised: pure tilt (Fig. 1c) and pure twist (Fig. 1d) boundaries.

94 Pure tilt intragranular boundaries (Fig. 1c) develop by the progressive addition of, in principal, a  
95 single set of edge dislocations to achieve the misorientation between adjacent domains (e.g.  
96 Burgers, 1939a, b and 1940; Buranova, 1940; Shockley and Read, 1949; Read and Shockley, 1950).

97 A rotation angle ( $\omega$ ) and axis ( $r$ ) can therefore be recognised. As the rotation axis lies within the  
98 boundary plane and hence perpendicular to the boundary plane normal ( $h$ ; Fig. 1c),

$$99 \quad r \cdot h = 0 \quad (3)$$

100 In contrast, pure twist intragranular boundaries (Fig. 1d) develop via (at least) two sets of (not  
101 necessarily orthogonal) screw dislocations to achieve the misorientation between adjacent domains  
102 (e.g. Bragg, 1940; Burgers, 1940; Shockley and Read, 1949; Read and Shockley, 1950). In this  
103 case, the rotation axis is perpendicular to the boundary plane and hence parallel to its normal, such  
104 that,

$$105 \quad r \cdot h = 1 \quad (4)$$

106 In practice most boundaries are probably combinations of tilt and twist components necessary to  
107 create the ‘best-fit’ between adjacent domains. Thus,

$$108 \quad 0 \text{ (pure tilt)} \leq \text{TTC} \leq 1 \text{ (pure twist)} \quad (5)$$

109 where TTC is the vector product of the rotation axis ( $r$ ) and boundary plane normal ( $h$ ) and is  
110 known as the boundary tilt-twist component index (Amouyal et al., 2005). However, and in spite of  
111 the apparent simplicity of Eqns 3 – 5, a boundary separating two adjacent misoriented crystal  
112 lattices can have an effectively infinite number of physical orientations, defined by its planar  
113 normal (Fig. 1b - d). Herein lies the inherent problem and concomitant requirement for defining the  
114 complete five-parameter orientation of intragranular boundaries.

115 In this contribution, we propose a simple practical solution for the definition of the five-parameter

116 orientation of intragranular boundaries. Our solution arises from the recognition that all  
117 intragranular boundaries involve four common geometrical parameters (Fig. 1): boundary trace ( $t$ ),  
118 boundary plane normal ( $h$ ), rotation axis ( $r$ ) and rotation angle ( $\omega$ ). In addition, the basic  
119 requirement involves knowledge of the crystallographic orientation of the domains on either side of  
120 a boundary, as well as the (crystallographic) orientation of the boundary plane normal direction.  
121 Whilst we derive our solution from original observations made via SEM back-scattered electron  
122 (BSE) electron channelling (EC), we subsequently demonstrate not only how it can be adapted for  
123 EBSD data but also suggest how it may be extended to (some) intergranular boundaries.

## 124 **2. METHOD**

### 125 **2.1 Electron channelling**

126 SEM/EC (e.g. Hirsch et al., 1962; Venables and Harland, 1973; Joy, 1974; Goldstein and Yakowitz,  
127 1975; Joy et al., 1982) is a related technique to SEM/EBSD (e.g. Dingley, 1989; Prior et al. 1999  
128 and 2009) for determining crystallographic orientations via electron channelling patterns (ECP)  
129 rather than EBSD patterns. It also provides images based on sample crystallographic microstructure  
130 via BSE ‘orientation contrast’ (OC), also known as electron or orientation channelling contrast  
131 imaging (ECCI/OCCI) in recent literature (e.g. Zaefferer and Elhami, 2014); such images (e.g. Fig.  
132 2a) are equivalent to EBSD fore-scattered electron (FSE) images. The principal differences between  
133 EC and EBSD patterns are as follows.

134 (1) In EBSD, a vertical electron beam strikes a sample tilted at  $\sim 65\text{-}70^\circ$ , whereas for EC a vertical  
135 electron beam is rocked about a fixed point on a horizontal sample. (2) The angular spread of  
136 patterns can approach  $\sim 100^\circ$  in EBSD (Fig. 2b, c) but is typically only up to  $\sim 24^\circ$  in EC (Fig. 2d, e),  
137 as determined by the rocking angle ( $\pm RA$ ) of the incident electron beam; it is much easier therefore  
138 to identify (index) EBSD patterns, particularly via automation and in phases with low crystal  
139 symmetry. (3) However, the smaller angular spread for ECP results in better angular resolution

140 compared with EBSD patterns (Fig. 2b-e). (4) In contrast, the maximum spatial resolution of ECP  
 141 formation is from 1 - 10 $\mu$ m due to aberrations in the SEM objective lens, which is at least an order  
 142 of magnitude greater than conventional EBSD. (5) Because ECPs are produced by rocking a  
 143 stationary electron beam about a point on the sample surface, a one-to-one relationship is

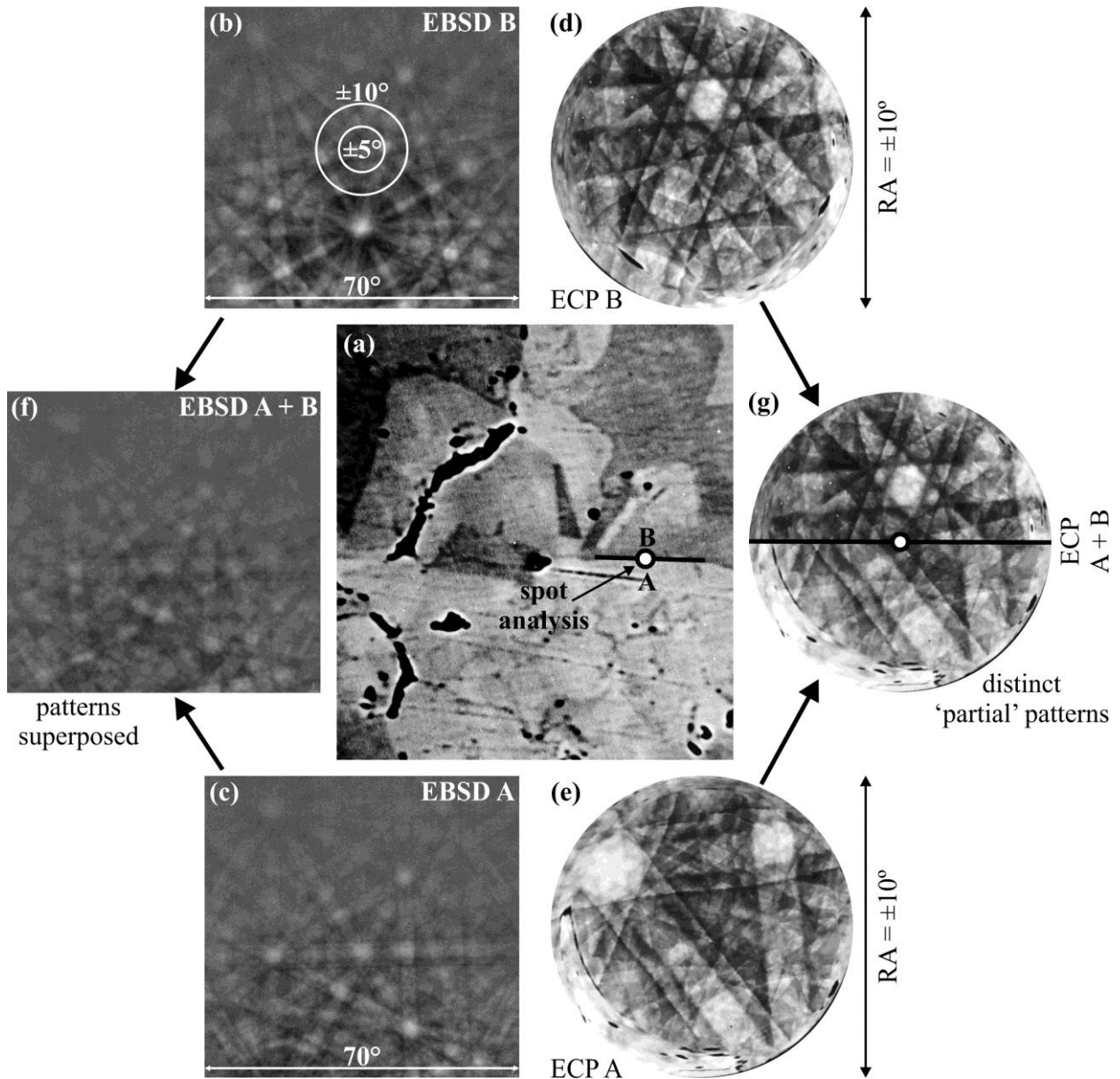


**Figure 2.** Comparison between electron backscattered diffraction (EBSD, left) and electron channelling (EC, right) patterns from pyrite. (a) EC orientation contrast (OC) and/or EBSD fore-scattered electron (FSE) image; note adjacent regions A and B separated by a distinct boundary. (b) and (c) Individual EBSD patterns from regions B and A respectively cover  $\sim 70^\circ$  of the crystal structure. (d) and (e) Individual EC patterns (ECP) from regions B and A respectively cover only  $\sim 20^\circ$  (i.e. electron beam 'rocking angle', RA, =  $\pm 10^\circ$ ) of the crystal structure. (f) The EBSD pattern from the boundary between A and B is formed by the complete superposition of patterns (b) and (c), resulting in an indistinct image. (g) The ECP from the boundary between A and B is composed of the relevant halves of patterns (d) and (e), resulting in a distinct image consisting of recognisable 'partial' patterns.

144 maintained between each point on the surface and in the pattern such that ‘partial’ ECPs  
 145 characteristic of the crystallographic orientation on each side of a boundary are produced (Fig. 2g);  
 146 this one-to-one relationship does not exist for EBSD patterns, which instead are superposed and  
 147 appear indistinct (Fig. 2f). It is this last characteristic that provides the crucial opportunity to  
 148 determine the complete orientation of intragranular boundaries.

## 149 **2.2 Boundary rotation angle(s) and axis**

150 Figure 3a is a schematic representation of partial ECP configurations across an intragranular  
 151 boundary (trace  $t$  and trace normal  $h_t$ ) and illustrates how the boundary tilt angle ( $\omega$ ) and axis ( $r$ )  
 152 can be determined. The crucial observation is to recognise the EC (diffraction) band (or crystal  
 153 lattice plane) that is not displaced across the boundary trace. This band ‘dips’ towards the pattern  
 154 centre by  $90-\beta^\circ$ . The value of  $\beta$  is determined via the internal scaling present in ECP formation,  
 155 which is constrained by the specific SEM operating conditions (i.e. accelerating voltage, working  
 156 distance, etc.) and indicated by RA (degrees/radians) and the pattern diameter ( $D$  mm), such that,

$$157 \quad \beta^\circ = B_{mm} \times 2RA^\circ/D_{mm} \quad (6a)$$

158 where  $B_{mm}$  is the orthogonal linear distance measured in the ECP between the non-displaced  
 159 channelling band and the pattern centre (Fig. 3a). Similar calculations can be defined for all other  
 160 EC bands and angular distances.

161 For the EC band to be non-displaced, the displacement translation vector ( $d_v$ ) must be contained  
 162 within the band (Fig. 3b). Thus, the normal to the non-displaced EC band must be parallel to the  
 163 boundary rotation axis. As well as the non-displaced EC band, any bands parallel to the boundary  
 164 trace are also recognised. The ECP configuration prior to boundary formation can be restored by  
 165 translating one partial pattern relative to the other, parallel to the displacement translation vector of  
 166 the non-displaced EC band until all bands become aligned (Fig. 3b). The boundary rotation angle  
 167 ( $\omega_r$ ) is then obtained from the displacement distance ( $d$ ) in a similar manner to Eqn 6a,

$$168 \quad \omega_r^\circ = d_{mm} \times 2RA^\circ/D_{mm} \quad (6b)$$

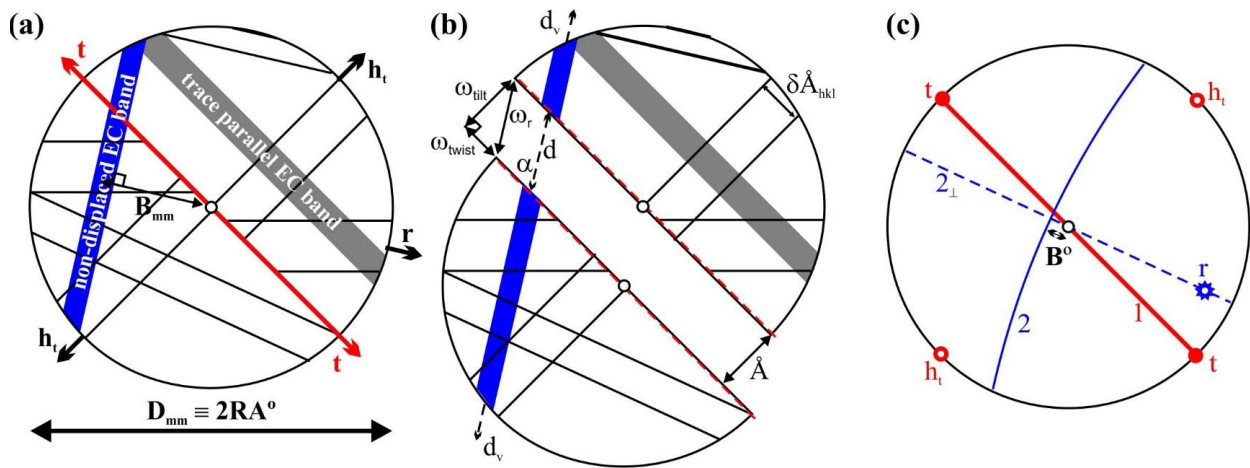


**Figure 3.** Determination of boundary rotation axis and angles. (a) Schematic partial ECPs across an intragranular boundary (t, trace; h<sub>t</sub>, trace normal). The normal to the non-displaced EC band, which ‘dips’ 90-β° where β = BxD/2RA (B, linear distance from non-displaced band centre to pattern centre; D, twice the rocking angle), defines the direction of the boundary rotation axis (r). Note also a boundary trace parallel EC band. (b) Restoration of pre-boundary formation ECP configuration via the displacement vector (d<sub>v</sub>) parallel to the non-displaced EC band (α, acute angle between non-displaced band and boundary trace). Total rotation angle (ω<sub>r</sub>) is parallel to the displacement distance (d), with tilt (ω<sub>tilt</sub>) and twist (ω<sub>twist</sub>) components normal and parallel to the boundary trace (determined via internal scaling relative to RA and D); the tilt component can also be represented in terms of distance (Å) via internal scaling provided by EC bandwidth (δΔ<sub>hkl</sub>). (c) Upper hemisphere stereographic (Wulff/equal angle) and/or crystallographic projection representation: 1, boundary trace (t); 2, non-displaced EC band; 2<sub>⊥</sub>, vertical plane normal to non-displaced EC band; r, boundary rotation axis.

169 In the example shown in Fig. 3, the displacement vector is oblique to the boundary trace, which  
 170 indicates a general boundary. From Fig. 1, pure tilt displacements develop normal to the boundary  
 171 trace via rotation parallel to the trace, whereas pure twist displacements develop parallel to the trace  
 172 via rotation normal to it. The tilt (ω<sub>tilt</sub>) and twist (ω<sub>twist</sub>) angular components of a general boundary  
 173 can therefore be determined by resolving ω<sub>r</sub> into its boundary trace normal and parallel  
 174 displacements respectively,

$$175 \quad \omega_{\text{tilt}}^{\circ} = d \sin \alpha \ 2RA^{\circ} / D_{\text{mm}} \quad (6c)$$

$$176 \quad \omega_{\text{twist}}^{\circ} = d \cos \alpha \ 2RA^{\circ} / D_{\text{mm}} \quad (6d)$$

177 where α is the (acute) angle between the non-displaced EC band and the boundary trace (t).

178 The displacement normal to the boundary trace can also be expressed as a length (e.g. in angstroms,  
 179 Å) via the scaling provided by the width of the diffraction bands, which depends on the SEM

180 accelerating voltage used, and is readily available in EC/EBSD processing software. Figure 3c  
 181 summarises the boundary trace (1), non-displaced EC band (2), including its vertical normal plane  
 182 ( $2_{\perp}$ ), and rotation axis (r) orientations in terms of (Wulff/equal angle) stereographic and/or  
 183 crystallographic projections.

### 184 **2.3 Boundary plane orientation**

185 As stated previously, the main problem with defining the complete five-parameter orientation of  
 186 intragranular boundaries concerns the physical orientation of the boundary plane normal direction.  
 187 This is not a problem unique to intragranular boundaries. For example, the inclination ( $\psi$ ) of  
 188 boundaries formed during grain boundary sliding (gbs) can be determined from a relatively simple  
 189 relationship between the offsets of three mutually perpendicular directions (u, v, w) and the angle  
 190 ( $\theta$ ) between the trace of the boundary and a reference direction, such that (Langdon, 2006),

$$191 \quad \tan\psi = (u - w \tan\theta)/v \quad (7)$$

192 However, it is impractical to use this equation (e.g. in the determination of the contribution of gbs to  
 193 the total strain) because of the difficulties of measuring the angles  $\theta$  and  $\psi$  at every boundary  
 194 (Langdon, 2006; Mohamed, 2011). Similarly, the movement characteristics of geological faults  
 195 relies implicitly on knowledge of the dip of the fault plane (e.g. Redmond, 1972; Yamada and  
 196 Sakaguchi, 1995 Xu et al., 2007 and 2009; Lisle and Walker, 2013); if the dip is not known, it is  
 197 difficult to determine from other parameters except for specific combinations (e.g. Nieto-Fuentes et  
 198 al., 2014). Fortunately, the geometry of partial ECPs formed across a common intragranular  
 199 boundary (e.g. Fig. 3) offers a relatively simple practical solution to the problem.

200 The solution assumes implicitly that intragranular boundary orientations are constrained not only  
 201 crystallographically to low-index lattice planes (i.e. Read and Shockley, 1950) but also by the origin  
 202 of ECPs. Following Friedel's rule (Friedel, 1913), which introduces an effective centre of  
 203 symmetry, each EC band originates from the centre of a spherical projection directly below the  
 204 pattern centre defined by the rocking position (Fig. 4a). Thus, only bands 'steeper' than  $(90 - RA)^{\circ}$



210 The crux of our solution is that for intragranular boundaries constrained crystallographically to low-  
 211 index lattice planes, the trace of the boundary plane is parallel to an EC band ideally present in the  
 212 (partial) ECPs (e.g. Fig. 3a). However, as shown in Fig. 4c, there can be multiple possible solutions.  
 213 The problem therefore is to determine which specific lattice plane is parallel to the boundary plane.  
 214 In fact, the problem is even more complex as the boundary plane, although constrained to be  
 215 parallel to a low-index lattice plane, does not have to be coincident with that plane (e.g. Fig. 3a).  
 216 This is because all EC bands originate from the centre of a spherical projection (Fig. 4a), such that  
 217 the distance between the band and the centre of the ECP increases with inclination (Fig. 4c). In  
 218 contrast, intragranular boundaries are physical features that do not originate from the centre of the  
 219 spherical projection. Thus, whilst EC bands dipping  $<(90 - RA)^\circ$  do not appear in the ECP, a  
 220 mutually parallel intragranular boundary plane can still be observed in the image. Concomitantly, it  
 221 follows that straight boundary traces, including those through the centre of ECPs, are not  
 222 constrained to be vertical. The solution to the problem of determining the physical orientation of  
 223 intragranular boundaries is provided by stereographic projection analysis based on the geometry of  
 224 partial ECPs. Figure 3c shows the basic relationships between the boundary trace and its vertical  
 225 normal plane, the non-displaced EC band and its vertical normal plane, and the boundary rotation  
 226 axis plotted in (Wulff/equal angle) stereographic and/or crystallographic projections. We now  
 227 develop this construction in Fig. 5.

228 We first plot (Fig. 5a) the boundary trace (1), the non-displaced EC band (2) and their respective  
 229 vertical normal planes ( $1_\perp$ ,  $2_\perp$ ). The intersection (3) of the non-displaced EC band (2) and the  
 230 vertical section plane normal ( $1_\perp$ ) defines the pitch of the former on the latter. Next (Fig. 5b), we  
 231 construct small circles (4) with radii equal to the pitch (3) centred on the strikes (t) of the boundary  
 232 trace (1); these small circles define the loci of pitches of the boundary plane relative to the trace (t).  
 233 The intersections (5) of the small circles (4) with the vertical section plane normal to the non-  
 234 displaced EC band ( $2_\perp$ ) define the pitches of the boundary plane on that plane. The strikes (t) of the  
 235 boundary trace (1) and the small circle intersections (5) must lie in the boundary plane; the great

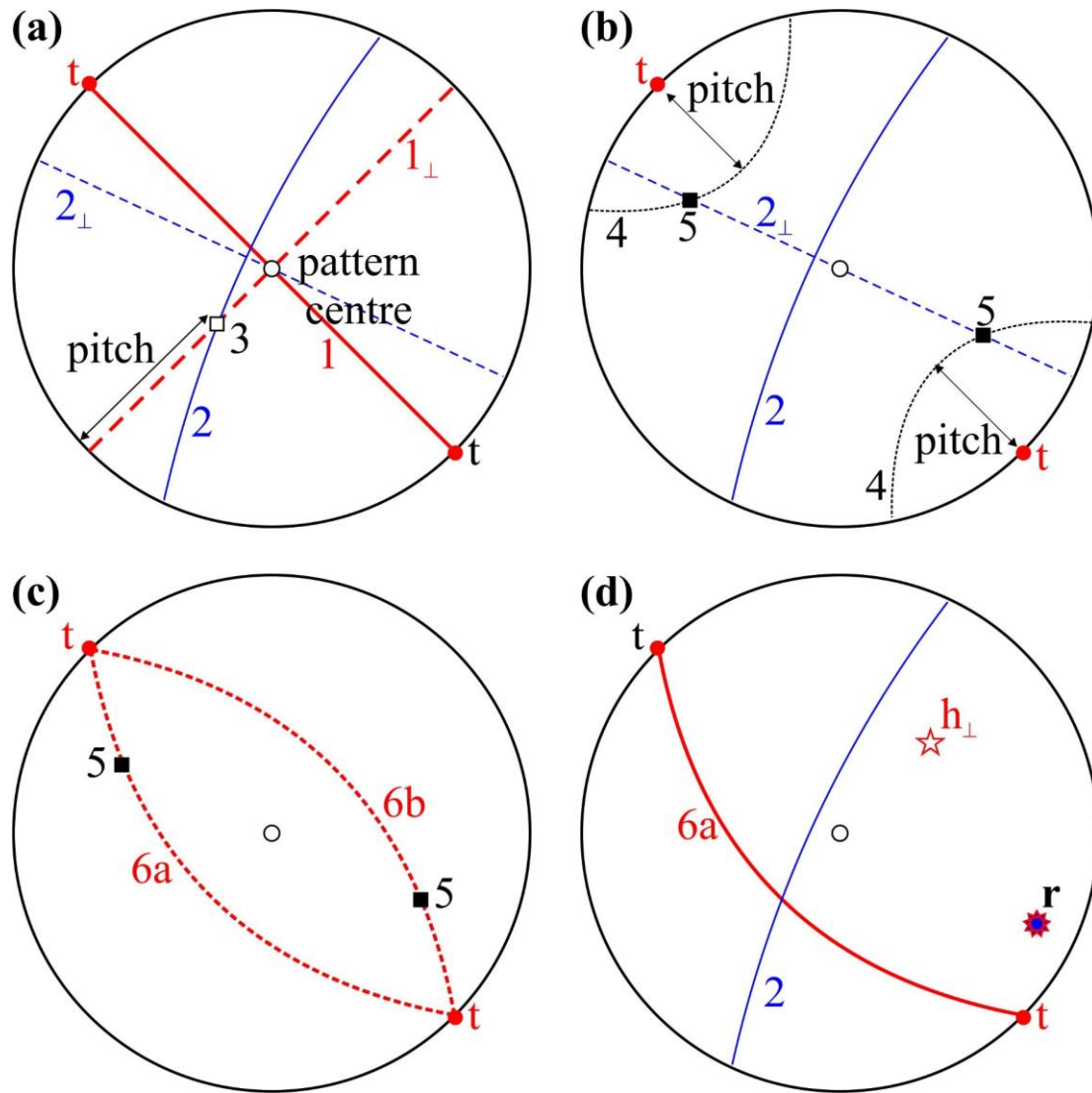


**Figure 5.** Determination of boundary plane orientation: red and blue colours indicate boundary plane and non-displaced EC band related elements respectively (see Fig. 3). (a) Plot of boundary trace (1), non-displaced EC band (2) and their respective vertical normal planes ( $1_{\perp}$ ,  $2_{\perp}$ ); intersection (3) of 2 and vertical  $1_{\perp}$  defines the pitch of the former on the latter. (b) Small circles (4) with radii equal to the pitch (3) constructed about strikes (t) of the boundary trace (1); the small circles define the loci of the pitches of the boundary plane and their intersections (5) with the vertical section plane normal to the non-displaced EC band ( $2_{\perp}$ ) define the pitches of the boundary plane on that plane. (c) Strikes (t) of boundary trace (1) and small circle intersections (5) must lie in the boundary plane, such that great circles (6a, b) through these points define its potential orientations; the most likely alternative is determined by coincidence between the planes and any EC band in the partial ECPs (e.g. Fig. 3a). (d) Determination of non-displaced EC band normal (r, boundary rotation axis) and boundary plane normal ( $h_{\perp}$ ) directions.

236 circles (6a, b) through these points therefore define its two alternative orientations (Fig. 5c). To  
 237 choose the most likely alternative, we check for coincidence between the predicted boundary planes  
 238 and any low-index boundary-parallel EC band (e.g. Fig. 3a); we show below that this identification  
 239 is facilitated by spherical Kikuchi maps (SKM). Finally (Fig. 5d), the non-displaced EC band

240 normal ( $r$ ), which defines the boundary plane rotation axis, and boundary plane normal ( $h_{\perp}$ )  
241 directions are plotted. The crystal indices of these positions,  $[uvw]_r$  and  $[uvw]_{h_{\perp}}$ , are the values that  
242 should be used in Eqn. 4 to calculate the TTC component of the boundary.

243 In the next section, we provide actual examples of the application of the method to intragranular  
244 boundaries in olivine. The examples were imaged at the University of Leeds using a Tescan Vega3  
245 SEM operated in EC mode using a 25kV accelerating voltage, a specimen working distance of 9mm  
246 and rocking angles of  $\pm 10$ - $11^{\circ}$ ; beam currents were varied to obtain the best OC and ECP images.

### 247 3. EXAMPLE RESULTS

248 Figure 6a is an EC orientation contrast image of a single forsteritic olivine (orthorhombic, space  
249 group Pbnm) grain from a sample of volcanic ejecta (Kahl et al., in prep.); note the intragranular  
250 boundary comprising long, straight and short, kinked segments. Also shown are ECPs (1 and 2)  
251 from each side of the boundary (Fig. 6b, c). Whilst the patterns are slightly different due to the  
252 misorientation introduced by the boundary (e.g. compare their respective Euler angle triplets), their  
253 individual configurations are consistent along each side of the boundary irrespective of the  
254 (boundary) segment orientation. Figures 6d and e show partial ECPs from each side (1 and 2) of the  
255 two boundary segments respectively, obtained by rocking the incident electron beam on the  
256 boundary as indicated. The boundary traces are clearly observed in both images by displacement of  
257 EC bands. The displacement sense is either sinistral or dextral depending on the orientation (i.e.  
258 angle of intersection) of the EC band relative to the boundary trace. However, one EC band towards  
259 the upper left, which is the same for both boundary segments, is continuous across the boundary.

260 Spherical geometry dictates that the inclination ('dip') of any EC band is the (angular) distance  
261 between the normal to the band, measured from the band centre, and the centre of the pattern  
262 subtracted from  $90^{\circ}$  (Eqn 6). All bands 'dip' towards the pattern centre (i.e. the centre of the

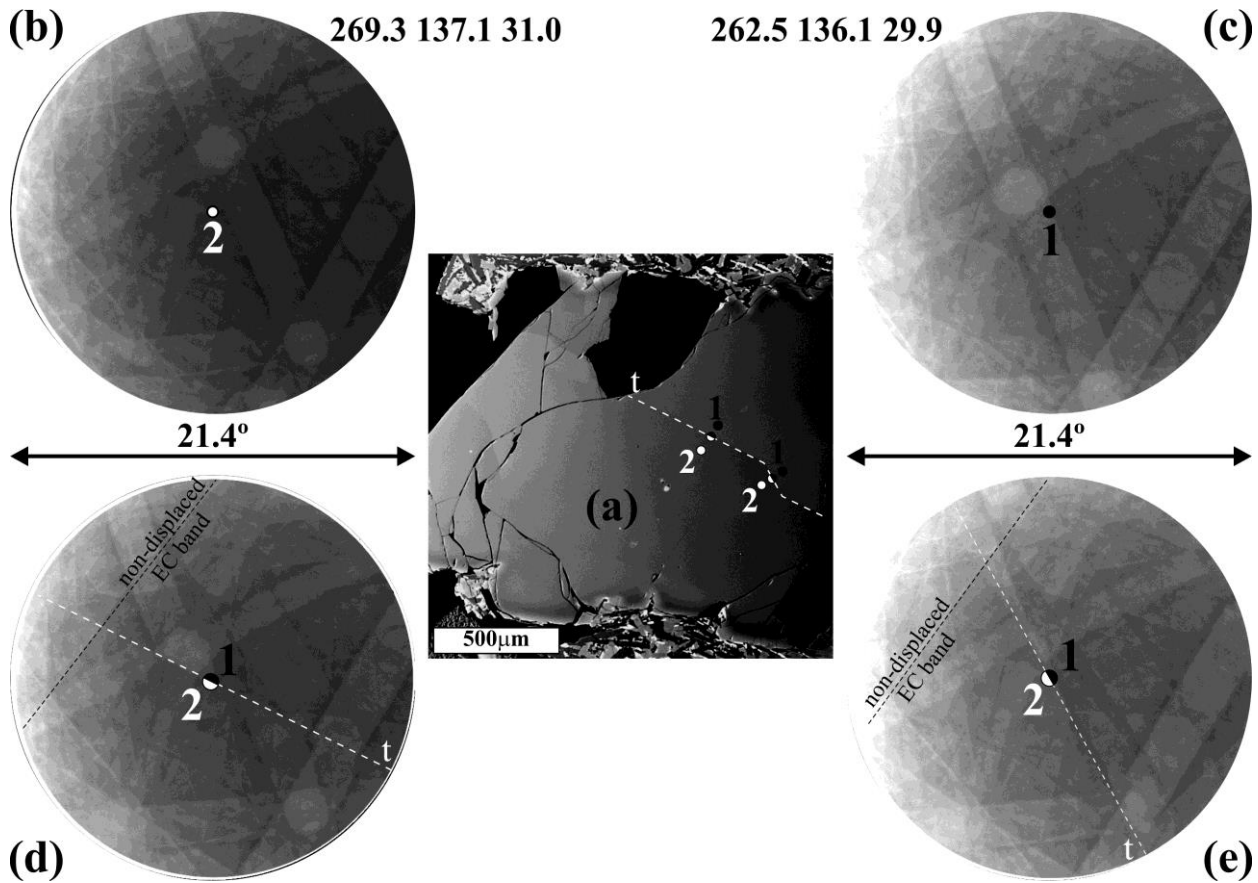


**Figure 6.** Intragranular boundary orientation method example. (a) Olivine grain with intragranular boundary comprising long, straight and short, kinked segments (electron channelling orientation contrast). (b) and (c) Complete electron channelling patterns from points 1 and 2 either side of the boundary (note Euler angle triplets); the patterns and hence orientations do not change along the boundary segments. (d) and (e) Partial electron channelling patterns from the long, straight (d) and short, kinked (e) boundary segments (broken white lines); note displacement of all channelling bands except for one, which is the same for both segments.

263 spherical projection, which is therefore upper hemisphere). Scaling is provided by the rocking angle  
 264 involved in pattern formation, which is  $RA = \pm 10.7^\circ$  for this example.

### 265 3.1 Boundary rotation angles and axes

266 The rotation angles and axes for the two olivine intragranular boundary segments (Fig. 6) are  
 267 determined following the procedure outlined above (Fig. 3), illustrated in Figs 7a, b and 8a, b.

268 Based on the orthogonal distances from the centres of the non-displaced band to the rocking  
 269 positions (i.e. pattern centres), it is inclined at  $81.8^\circ$  and  $82.2^\circ$  towards the pattern centres

270 respectively for the two segments. As the normal to the non-displaced EC band defines the

271 orientation of the boundary plane rotation axis, this must be the same crystallographically for both

272 boundary segments irrespective of the different orientations of their boundary traces and hence  
 273 planes. The rotation axes for the two segments therefore plunge 8.2° and 7.8° respectively normal to  
 274 the non-displaced band.

275 The rotation angles associated with formation of the two intragranular boundary segments can be  
 276 determined by translating one of the partial patterns parallel to the non-displaced EC band until all  
 277 of the other EC bands become continuous (Figs 7b and 8b). In other words, the effect of the  
 278 intragranular boundary has been ‘removed’. In the examples shown, the translation directions are  
 279 not orthogonal to the trace of either boundary segment, indicating that both segments are general  
 280 boundaries and that the overall rotation angle ( $\omega$ ) comprises both tilt ( $\omega_{\text{tilt}}$ ) and twist ( $\omega_{\text{twist}}$ )  
 281 components.

282 The overall rotation angle is defined by the (angular) separation of the partial patterns along the  
 283 displacement vectors, according to the internal scaling present in the ECPs (i.e. RA = ±10.7°) and  
 284 using Eqn 6. The tilt and twist components are the displacements respectively normal and parallel to  
 285 the boundary trace such that,

$$286 \quad \omega = (\omega_{\text{tilt}}^2 + \omega_{\text{twist}}^2)^{1/2} \quad (8)$$

287 In terms of the long, straight segment,  $\omega = 3.3^\circ$ , with  $\omega_{\text{tilt}} = 3.1^\circ$  and  $\omega_{\text{twist}} = 1.0^\circ$  (Fig. 7b); whilst  
 288 for the short, kinked segment,  $\omega = 2.6^\circ$ , with  $\omega_{\text{tilt}} = 2.2^\circ$  and  $\omega_{\text{twist}} = 1.4^\circ$  (Fig. 8b). As recognised  
 289 previously, both segments are general boundaries. However, by comparing the relative values of the  
 290 tilt and twist components for each segment, the long, straight segment involves significantly more  
 291 tilt than twist in its configuration. To quantify the boundary segments more precisely (e.g. by the  
 292 TTC index) requires accurate definition of their boundary plane orientations.

### 293 **3.2 Boundary plane orientations**

294 To determine the orientation of the two boundary plane segments (Fig. 6a), we follow the workflow  
 295 outlined in Fig. 5. First, we plot (Figs 7c and 8c) Wulff/equal angle upper hemisphere stereographic

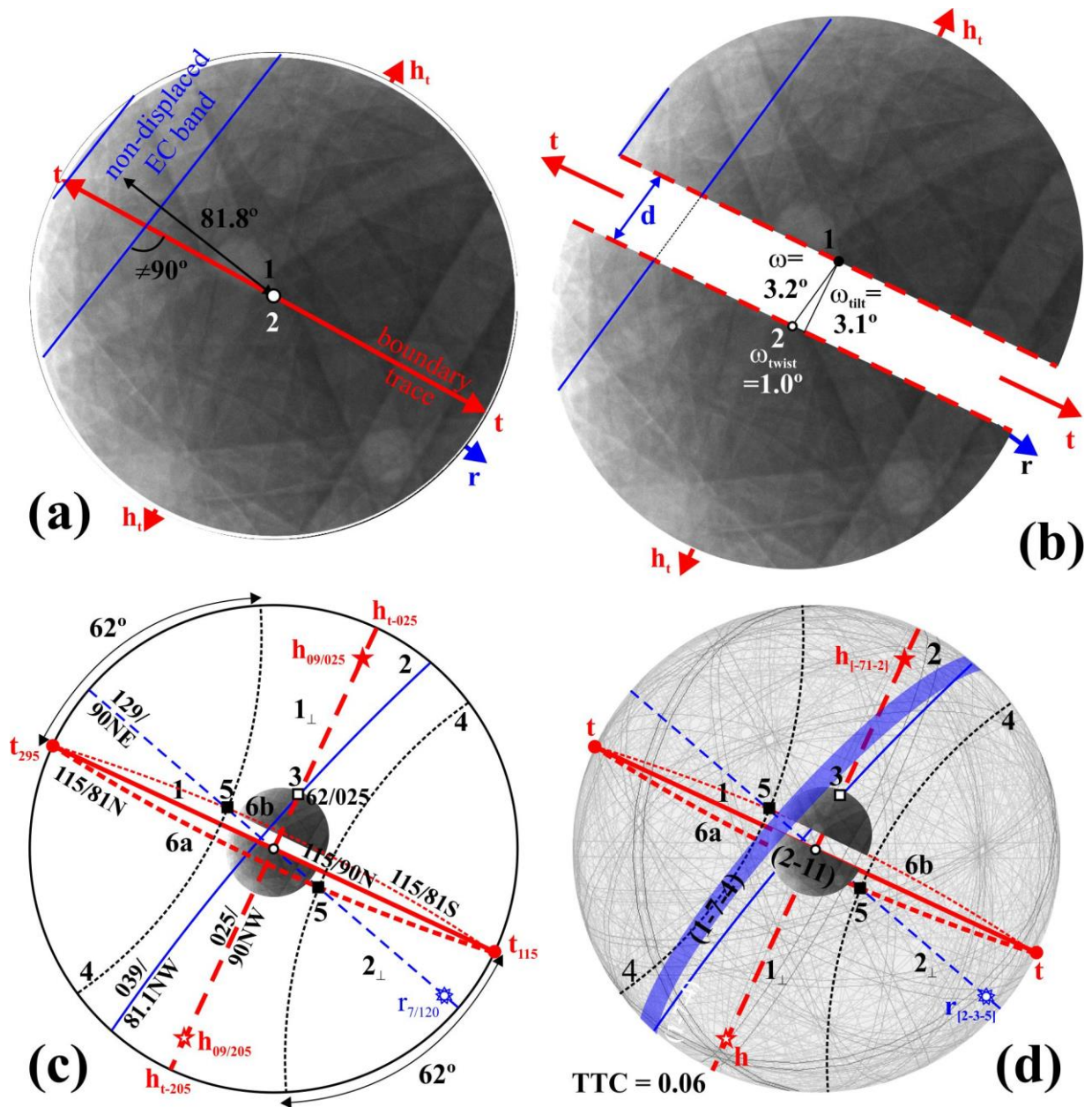


**Figure 7.** Intragranular boundary orientation determination: olivine long, straight segment (see Fig. 6). Nomenclature and colours as in Figs 3 and 5. (a) Partial ECPs from across the boundary segment ( $t$ , trend and  $h_t$ , trend normal); all EC bands are displaced across the boundary except one (indicated, with ‘strike/dip/sense’); normal to this band defines boundary rotation axis ( $r$ , 09/129 ‘plunge/azimuth’). (b) Partial ECPs ‘restored’ to pre-boundary formation positions by translation parallel to non-displaced EC band such that all bands are continuous. The translation distance is the boundary rotation angle ( $\omega$ ), which can be resolved into its boundary normal tilt ( $\omega_{\text{tilt}}$ ) and boundary parallel twist ( $\omega_{\text{twist}}$ ) components for general boundaries. (c) Stereographic projection (*upper hemisphere, Wulff/equal angle*) of progressive steps involved in boundary orientation determination (see Fig. 5 and associated text for definition of numbers/symbols). Two symmetrical solutions are indicated, both ‘striking’  $115^\circ$  and ‘dipping’ either  $81^\circ\text{N}$  or  $81^\circ\text{S}$ . (d) Spherical Kikuchi map (SKM) representation illustrating crystallographic indexing procedure and final selection of boundary plane orientation (115/81N) based on coincidence with (2-11) EC band/lattice plane. Note also crystallographic orientations of  $r$  and  $h$  (i.e. true boundary plane normal), allowing determination of  $\text{TTC} = 0.17$ , close to a pure tilt intragranular boundary.

297 projections of the orientations of the boundary trace (1), its (vertical) normal plane ( $1_{\perp}$ ), the non-  
298 displaced EC band (2) and its (vertical) normal plane ( $2_{\perp}$ ). The values are determined using Eqn 6  
299 ( $0 - 90^{\circ}$ ) and the clockwise azimuthal direction around the pattern circumference ( $0 - 180^{\circ}$ ). Next,  
300 we determine the intersection (3) of the non-displaced EC band on the (vertical) normal to the  
301 boundary segment trend; the intersection defines the loci of the pitches of the boundary plane as  
302 small circles (4) about the strike (t) of the boundary trace (1). The intersections (5) of the small  
303 circles (4) with the vertical section plane normal to the non-displaced EC band ( $2_{\perp}$ ) define the  
304 pitches of the boundary plane on that plane. The strikes (t) of the boundary trace (1) and the  
305 intersections (5) must lie in the boundary plane; great circles through these points therefore define  
306 its potential orientations (6).

307 Typically, two alternative and symmetrical grain boundary plane solutions are obtained (6a and 6b).  
308 To choose the most likely alternative, we check for coincidence between the predicted boundary  
309 plane orientations and an EC band by overlaying the partial ECPs onto the stereographic projection  
310 (Figs 7c and 8c). This is because the dislocation model for intragranular boundary formation  
311 predicts that they coincide with low index crystal planes. For the long, straight segment, alternative  
312 6a oriented  $115^{\circ}/81^{\circ}\text{N}$  is coincident with an EC band that is parallel to the boundary trace (see Figs  
313 6b-d and 7a, b), which is therefore selected. For the short, kinked segment, alternative 6a oriented  
314  $158^{\circ}/83^{\circ}\text{W}$  is also coincident with an EC band that is parallel to the boundary trace (see Figs 6b-d  
315 and 8a, b), which is therefore selected. Having selected the appropriate boundary plane orientations,  
316 the boundary plane normal directions ( $h_{\perp}$ ) can be determined for both segments.

317 Figures 7c and 8c define the boundary segment orientations in terms of spherical angles. As such,  
318 they are measured and represented in terms of the sample coordinate system. In this example, the  
319 olivine grain is from a sample of volcanic ejecta and consequently has no specific specimen  
320 orientation. It would be useful therefore to express the boundary segment plane orientations in  
321 terms of (olivine) crystallography. This is possible by use of spherical Kikuchi maps (SKM; see



323 Day 2008 and 2009) and in particular the interactive versions for olivine available in the HKL  
 324 Channel5 and/or AZtecCrystal software packages (Fig 7d and 8d). In effect, the stereographic  
 325 projection construction is simply overlain onto an SKM defined by the orientation of the ECPs,  
 326 either via visual comparison or, more accurately, via their Euler angle triplets (e.g. Figs 6a, b);  
 327 however, care is required beyond 45° from the centre of projection due to increasing spherical  
 328 distortion. It is also possible to incorporate the ‘restored’ partial ECPs into the construction (Figs 7d  
 329 and 8d). The interactive nature of the SKM then makes it a simple matter to index  
 330 crystallographically the relevant planes and direction.

331 Based on the olivine SKM, the non-displaced EC band common to both boundary segments is the  
 332  $(1\bar{7}\bar{4})$  lattice plane (Figs 7d and 8d). The long, straight boundary segment is parallel to the  $(2\bar{1}1)$   
 333 lattice plane, whilst the short, kinked boundary segment is parallel to the  $(222)$  lattice plane.  
 334 However, a problem arises in the determination of the normal directions to these lattice planes due  
 335 to non-cubic (i.e. orthorhombic) symmetry relationships. We resort therefore to relationships  
 336 involving the reciprocal (orthorhombic) crystal lattice and metric tensor (e.g. Bond, 1976; Boisen  
 337 and Gibbs, 1990; De Graf and McHenry, 2012),

$$338 \quad M^* = \begin{bmatrix} a^* & 0 & 0 \\ 0 & b^* & 0 \\ 0 & 0 & c^* \end{bmatrix} \quad (9)$$

339 where  $a^* = bc/V$ ,  $b^* = ac/V$  and  $c^* = ab/V$ ;  $a = 4.76\text{Å}$ ,  $b = 10.21\text{Å}$  and  $c = 5.98\text{Å}$  are the orthogonal  
 340 olivine lattice parameters; and  $V = abc$  is the volume of the olivine unit cell ( $290.38\text{Å}^3$ ). The  
 341 direction  $[uvw]$  normal to the plane  $(hkl)$  is then given by,

$$342 \quad \begin{bmatrix} u \\ v \\ w \end{bmatrix} = M^* \begin{pmatrix} h \\ k \\ l \end{pmatrix} \quad (10)$$

343 Thus, the rotation axis normal to the  $(1\bar{7}\bar{4})$  non-displaced lattice plane is parallel to  $[2\bar{3}\bar{5}]$ , whilst  
 344 the normal directions to the  $(2\bar{1}1)$  and  $(222)$  boundary parallel lattice planes are parallel to  $[7\bar{1}2]$   
 345 and  $[513]$  respectively. Combining the common rotation axis with the boundary plane normal

<b>Table 1. Summary of olivine boundary parameters (Figs. 6 - 8)</b>		
<b>Boundary Parameter</b>	<b>long, straight segment</b>	<b>short, kinked segment</b>
non-displaced EC band	(174)	(174)
rotation axis plunge/trend	08°/129°	08°/129°
rotation axis (r)	<b>[235]</b>	<b>[235]</b>
boundary plane	(211)	(222)
boundary trend (t)	115°/295°	158°/328°
boundary plane normal plunge/trend	09°/025° or 205°	10/068° or 248°
boundary plane normal (h)	<b>[712]</b>	<b>[513]</b>
rotation angle ( $\omega$ )	<b>3.3°</b>	<b>2.6°</b>
<i>tilt component (<math>\omega_{tilt}</math>)</i>	3.1°	2.2°
<i>twist component (<math>\omega_{twist}</math>)</i>	1.0°	1.4°
tilt-twist component (TTC)	0.17	0.45
'excess volume' nm	25.16	8.87
<b>numbers in bold represent five-parameter definition of intragranular boundary orientations</b>		

346 directions yield TTC values of 0.17 for the long, straight boundary segment and 0.45 for the short,  
 347 kinked boundary segment. The former is defined as close to a pure tilt boundary whilst the latter is a  
 348 general boundary.

### 349 **3.3 Summary**

350 Table 1 summarises the results of the olivine intragranular boundary analyses (Figs 6 – 8) in terms  
 351 of both the sample (i.e. stereographic projection plane and normal orientations) and crystallographic  
 352 (i.e. crystal planes and normals) coordinate systems. The former is not representative for this  
 353 example as the sample does not possess a rigorous spatial orientation as it is a sample of volcanic  
 354 ejecta; however, this representation may be useful in samples that are kinematically constrained.  
 355 The latter represents the complete five-parameter determination of boundary plane orientations and  
 356 is constrained by the orthorhombic crystal structure of olivine. For example, the crystallographic  
 357 orientations can be represented in terms of conventional upper and/or lower hemisphere  
 358 orthorhombic projections (Fig. 9a, b).

## 359 **4. DISCUSSION**

360 In this section we discuss the implications of the model derived to determine the complete  
 361 orientation of intragranular boundaries. In combination with the results from the example (Figs 6 -

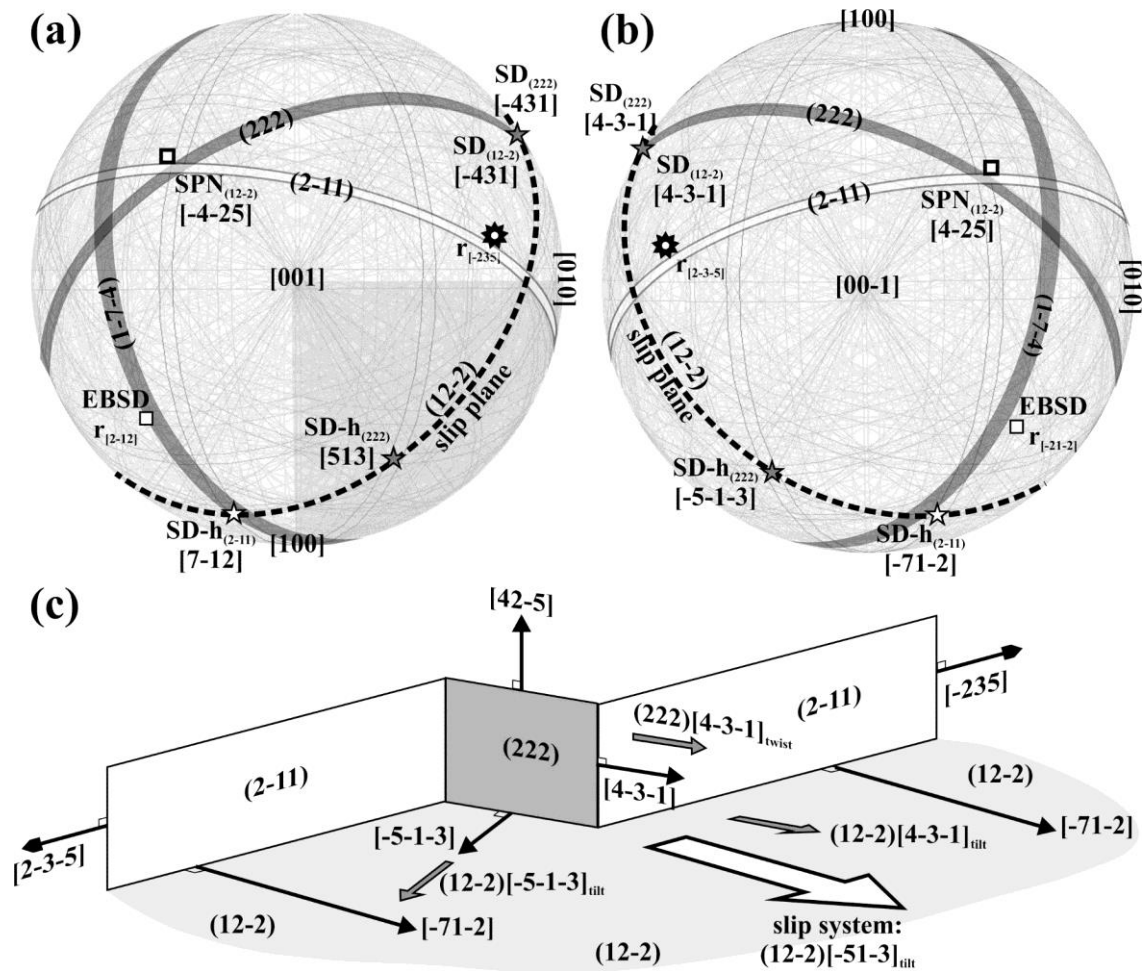


**Figure 9.** (a) Upper and (b) lower hemisphere SKM orthorhombic projections of the olivine intragranular boundary parameters determined by the method developed in this contribution. Also indicated are predicted crystal slip plane and directions for boundary formation as well as the misorientation axis determined by conventional EBSD analysis. (c) Schematic representation of olivine tilt and general boundary configuration and associated crystal planes, directions and slip systems.

362 8), we consider: (1) intragranular boundary formation and crystal slip system determination; (2)  
 363 conventional (i.e. EBSD-based) misorientation analysis; (3) adapting the EC-based method for  
 364 EBSD analysis; and (4) the applicability of the method for intergranular boundaries. To assist in this  
 365 discussion, we have summarised Table 1 in Table 2 to compare the olivine five-parameter boundary  
 366 definitions (Figs 6 - 8) with slip system determination and EBSD misorientation analysis.

#### 367 4.1 Intragranular boundary formation – slip systems

368 The long, straight and short, kinked segments shown in Fig. 6a are clearly part of the same olivine

<b>Table 2. Comparison of olivine five-parameter boundary definitions (Figs 6 -8), including slip systems, with EBSD misorientation analysis</b>									
	<b>Five parameter definition</b>					<b>Slip system</b>		<b>EBSD misorientation</b>	
<b>Boundary</b>	<b>h(hkl)</b>	<b>h[uvw]</b>	<b><math>\omega</math></b>	<b>r</b>	<b>TTC</b>	<b>SP</b>	<b>SD</b>	<b><math>\omega</math></b>	<b>r</b>
Long, straight	( $2\bar{1}1$ )	[ $7\bar{1}2$ ]	3.3°	[ $2\bar{3}5$ ]	0.17	( $12\bar{2}$ )	[ $7\bar{1}2$ ]	6.13°	[ $2\bar{1}2$ ],
Short, kinked	(222)	[513]	2.6°	[ $2\bar{3}5$ ]	0.45	( $12\bar{2}$ ) ( $12\bar{2}$ ) (222)	[ $5\bar{1}3$ ] [ $4\bar{3}1$ ] [ $4\bar{3}1$ ]		

369 intragranular boundary. They share the same boundary rotation axis of [ $2\bar{3}5$ ] in spite of their  
370 different boundary plane orientations, which are parallel to ( $2\bar{1}1$ ) and (222) respectively (Fig. 9c).  
371 However, the former is close to a pure tilt boundary (TTC = 0.17), whilst the latter is a general  
372 boundary (TTC = 0.45). The segments also differ in terms of their rotation angles, which is larger  
373 for the long, straight segment (i.e. 3.3° compared with 2.6°). This suggests that the long, straight  
374 segment represents the principal boundary and that the short, kinked segment is a minor component  
375 that may well have been removed with further boundary evolution.

376 In terms of intragranular boundary formation, we have assumed the standard Reed and Shockley  
377 (1950) dislocation model. Pure tilt boundaries, such as ( $2\bar{1}1$ ), form parallel to the boundary rotation  
378 axis and normal to the slip plane and slip direction. The slip direction is therefore normal to the  
379 boundary plane (Fig. 9c). From Eqn. 10, the boundary plane normal is determined to be [ $7\bar{1}2$ ], such  
380 that the slip system responsible for boundary formation is ( $12\bar{2}$ )[ $7\bar{1}2$ ]. In contrast, the normal to the  
381 (222) short, kinked boundary plane is parallel to [ $5\bar{1}3$ ] suggesting slip on ( $12\bar{2}$ )[ $5\bar{1}3$ ] was involved  
382 in its formation. However, this is a general boundary, which require at least two slip systems to  
383 form; thus, ( $12\bar{2}$ )[ $5\bar{1}3$ ] can be regarded as the tilt component. For pure twist boundaries, the slip  
384 plane is parallel to the boundary plane, which is (222). The slip plane also contains the slip  
385 direction, although its precise orientation is not directly defined. We suggest that the twist slip  
386 direction is parallel to the intersection of the tilt boundary and the slip plane for the pure twist  
387 boundary, which is [ $4\bar{3}1$ ] (Fig. 9a, b). Thus, the twist component of the general boundary was  
388 accommodated by slip on (222)[ $4\bar{3}1$ ] (see Fig. 9c). Incidentally, the normal to the ( $12\bar{2}$ ) slip plane

389 is  $[42\bar{5}]$ , which is parallel to the intersection of the two boundary segment planes (Fig. 9).  
390 Consequently, the four slip systems either share or intersect with the same slip plane,  
391 namely  $(12\bar{2})$ .

#### 392 **4.2 Comparison with conventional (EBSD) misorientation analysis**

393 The olivine sample (Figs 6 - 8) has also been analysed via EBSD, which provides Euler angle  
394 triplets for each side of the intragranular boundaries (Fig. 6b, c). EBSD software typically includes  
395 misorientation analysis for specified pairs of Euler angle triplets. However, as the Euler angle  
396 triplets are effectively constant for each side of the boundary, only a single pair of triplets is  
397 required to determine a single misorientation angle/axis pair applicable to both long, straight and  
398 short, kinked segments. The angle/axis pair determined is  $6.13^\circ/[2\bar{1}2]$ , significantly different to the  
399 rotation angles and directions determined by the five parameter method (Table 2). The EBSD  
400 misorientation axis  $[2\bar{1}2]$  lies close to the non-displaced EC band  $(1\bar{7}\bar{4})$  and is oblique to both  
401 boundary segment planes/traces (Fig. 9a, b). The segments are therefore general boundaries with the  
402 same characteristics according to EBSD misorientation analysis.

403 It is clear from Table 2 and Fig. 9 that conventional (EBSD) misorientation angle/axis pair analysis  
404 is insensitive to boundary type and physical orientation. This is not surprising as its definition  
405 recognises only the axis about which one crystal lattice needs to be rotated to bring it into alignment  
406 with another (Fig. 1a); the orientation of the boundary is not involved. Thus, both segments have  
407 the same misorientation angle/axis pair. The only configurations for which the misorientation axis  
408 could potentially define boundary plane orientation are for pure tilt and twist boundaries; the axis is  
409 parallel to the boundary plane in the former and normal to the plane in the latter. However, there  
410 remain a large number of possible inclinations within either pure tilt or pure twist boundary planes  
411 for a given trend (Fig. 4c, d), which makes even these ideal situations undefinable via conventional  
412 misorientation analysis.

413 In the initial SEM/EBSD implementation of misorientation analysis (e.g. Mainprice et al., 1993;  
414 Lloyd et al., 1997), there was no requirement for two crystal lattices to be adjacent (i.e. share a  
415 common boundary), although usually the calculated misorientation ‘angle/axis’ pair relates to  
416 neighbouring or ‘correlated’ domains (Wheeler et al., 2001). Depending on crystal symmetry, there  
417 are several crystallographically related solutions for the misorientation angle/axis pair across an  
418 intragranular boundary. Convention dictates that the solution with the smallest angle is chosen,  
419 often referred to as the ‘disorientation’ (MacKenzie and Thomson, 1957; Hanscomb, 1958;  
420 MacKenzie, 1958; Warrington and Boon, 1975). However, an alternative approach recognises that  
421 the nearest low-index boundary axis solution defines the misorientation between adjacent lattices  
422 (e.g. Gourdet et al., 1998). The two approaches are not equivalent, which results in the distinction  
423 between coincidence site lattice (CSL) and low-order coincident axial direction (CAD)  
424 visualisations of boundary geometry (e.g. Warrington and Boon, 1975). It has been suggested (e.g.  
425 Cross and Randle, 2003) that an unambiguous analysis of intragranular boundary orientation  
426 involves consideration of the CAD solution rather than just the disorientation. The five parameter  
427 method derived in this contribution is most compatible with the CAD solution.

428 In fact, misorientation analysis angle/axis and five-parameter rotation angle/axis pairs are entirely  
429 different parameters. In the former they bring two crystal lattices into parallelism irrespective of  
430 whether or not the lattices share a common intragranular boundary (Fig. 1a), whereas in the latter  
431 they relate to the rotation between two originally identical crystal lattices due to the formation of an  
432 intragranular boundary (Fig. 1b-d). Thus, in misorientation analysis the misorientation axis is  
433 unconstrained by the boundary plane orientation and adopts an orientation that minimises the  
434 rotation angle between two adjacent crystal lattices. In contrast, in the five-parameter method not  
435 only is the boundary plane orientation of fundamental significance but also the dislocation model  
436 for intragranular boundary formation imposes constraints on boundary plane orientations. We  
437 suggest therefore that conventional EBSD misorientation analysis may involve ambiguity in terms  
438 of characterising intragranular boundary orientations.

### 439 4.3 Adaption to EBSD

440 The method developed to determine the five parameters needed to constrain the orientation of  
441 intragranular boundaries is based on observations made via SEM/EC (e.g. Figs 2d-g and 3).  
442 However, few SEM are currently capable of EC analysis and crystallographic orientation  
443 measurements are more typically made via EBSD (e.g. Fig. 2b, c). It would be useful therefore if  
444 the basic method could be adapted for EBSD-based analysis and data. A solution is provided via  
445 SKMs (e.g. Fig. 9a, b) and is illustrated using the olivine example described previously (Figs 6 - 8).

446 The adaption is as follows. (1) EBSD derived Euler angle triplets obtained from each side of a  
447 boundary are input into an SKM to produce maps centred on each orientation (Fig. 10a); the maps  
448 are copied into a vector drawing package. (2) Circles equivalent to ECP rocking angles (e.g.  $\pm 10^\circ$ )  
449 are drawn about the centre of each map to simulate ECPs from each side of the boundary and the  
450 trace of the boundary is drawn across the centre of each pattern; ‘cropping’ tools are used to extract  
451 the ‘ECPs’ from the SKM (Fig. 10b). (3) The extracted patterns are again ‘cropped’ and separated  
452 along the boundary traces to form simulated ‘partial ECPs’ (Fig. 10c). (4) The cropped patterns are  
453 joined in appropriate pairings to simulate partial ECPs obtained by rocking about a central point on  
454 their common boundary (Fig. 10d). (5) The non-displaced EC/lattice band is identified, from which  
455 all of the parameters needed to define the complete five- parameter orientation of the boundary can  
456 be measured and/or determined via stereographic projection as per the basic method (Fig. 10e).

457 The adapted solutions in Fig. 10e compare favourably with the original solutions in Figs 7 and 8.  
458 They can therefore be used to determine the crystallographic orientations of the intragranular  
459 boundary planes as shown in Fig. 9. Thus, the original EC-based method devised to determine the  
460 five-parameter evolution of Intragranular boundaries can be easily adapted to EBSD data, making

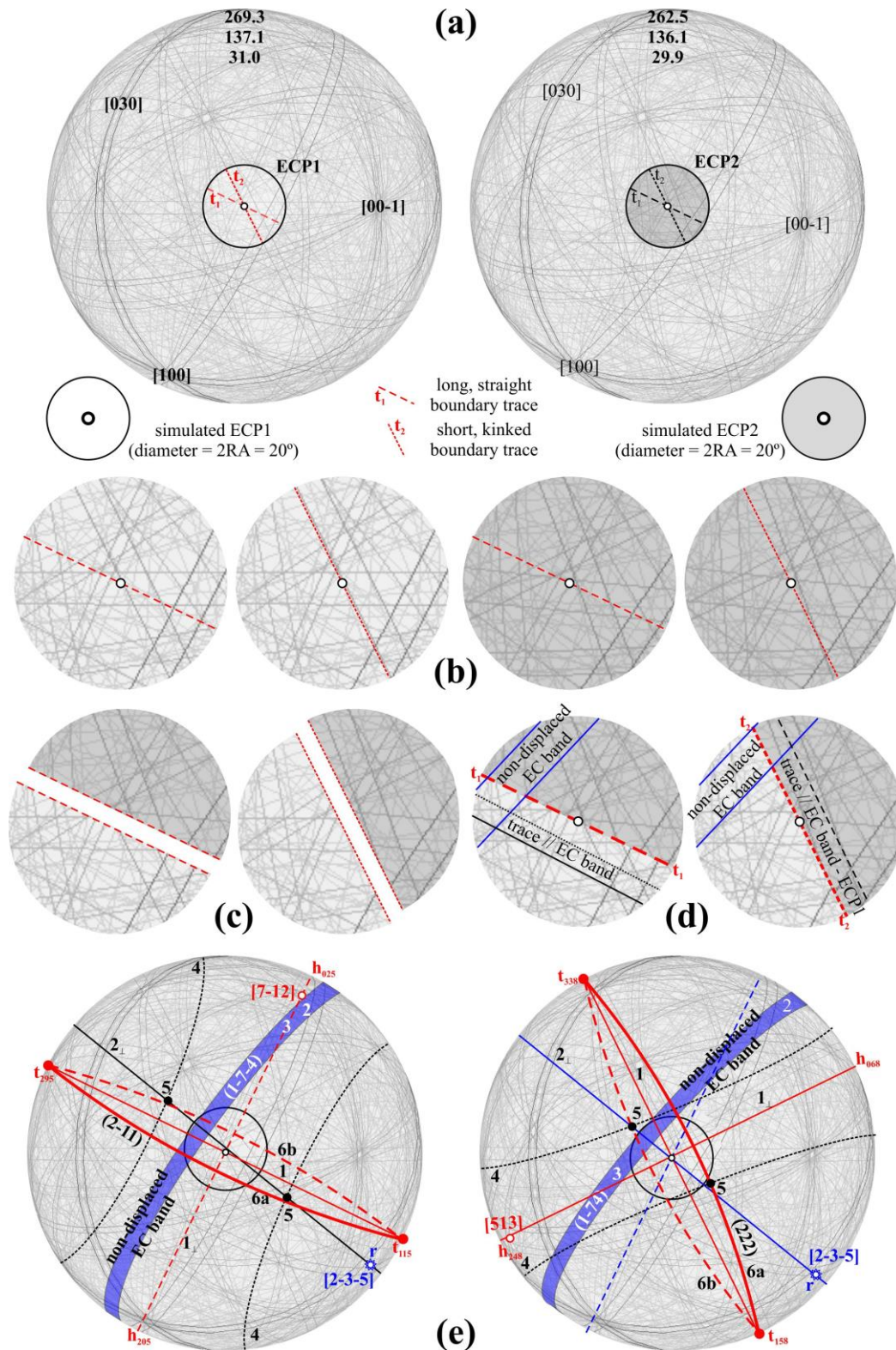


**Figure 10.** Adaption of the EC-based five-parameter boundary orientation method to EBSD data and analysis. Nomenclature and colours as in Figs 3 and 5. (a) *HKL Channel5*<sup>®</sup> SKMs defined by EBSD derived Euler angle triplets from each side of the olivine intragranular boundaries (Fig. 6). (b) Detail of SKM-simulated ECPs. (c) Simulated ECPs 'cropped' along boundary tracings. (d) 'Cropped' patterns joined appropriately along boundary traces to simulate partial ECPs formed by rocking about a point on the common boundary. (e) SKM representation of boundary orientation determination (1 – 6 refer to steps in the stereographic projection method, see Fig. 5): *left*, long, straight segment; *right*, short, kinked segment.

462 the approach more generally available.

#### 463 **4.4 Adaption to intergranular boundaries**

464 It is generally accepted (e.g. Rohrer, 2011) that the properties and behaviours of intergranular  
465 boundaries are controlled more by the physical geometry of the interfacial plane rather than  
466 crystallographic misorientation. This is because as misorientation increases so does dislocation  
467 density, which reduces space between neighbouring dislocations until their cores overlap such that  
468 the ordered nature of the boundary begins to break down. Unlike intragranular boundaries, which  
469 develop from a common initial crystal lattice by the progressive accumulation of dislocations (e.g.  
470 Reed and Shockley, 1950), there is no conventional *physical* reason why crystallographic  
471 relationships should exist across intergranular boundaries. In fact, the existence of such  
472 relationships may have significant implications for microstructural evolution. Thus, the method  
473 developed to determine the five-parameter orientation of intragranular boundaries should not  
474 necessarily be expected to apply to intergranular boundaries unless extenuating circumstances  
475 apply.

476 To investigate whether the method of determining the five-parameter orientation of intragranular  
477 boundaries can be adapted to intergranular boundaries, we consider the boundary relationships  
478 between a single olivine grain and its seven neighbouring olivine grains (Fig. 11a) in a garnet  
479 lherzolite from the 90 Ma Thaba Putsoa kimberlite, Lesotho (Nixon and Boyd, 1973; Mercier and  
480 Carter, 1985; Allsopp et al., 1989). The microstructure of this rock is characterised by a matrix of  
481 dynamically recrystallised olivine with straight grain boundaries and frequent 120° triple junctions,  
482 with a well-developed if somewhat unusual crystallographic preferred orientation (see Wallis et al.,  
483 2019). EBSD data were acquired at the University of Leeds using Oxford Instruments Aztec 2.1  
484 software on a FEI Quanta 650 field-emission gun SEM equipped with an Oxford Instruments  
485 Nordlys-S EBSD camera. Operating conditions were: 20kV accelerating voltage, 8mm working  
486 distance and 70° specimen tilt angle.

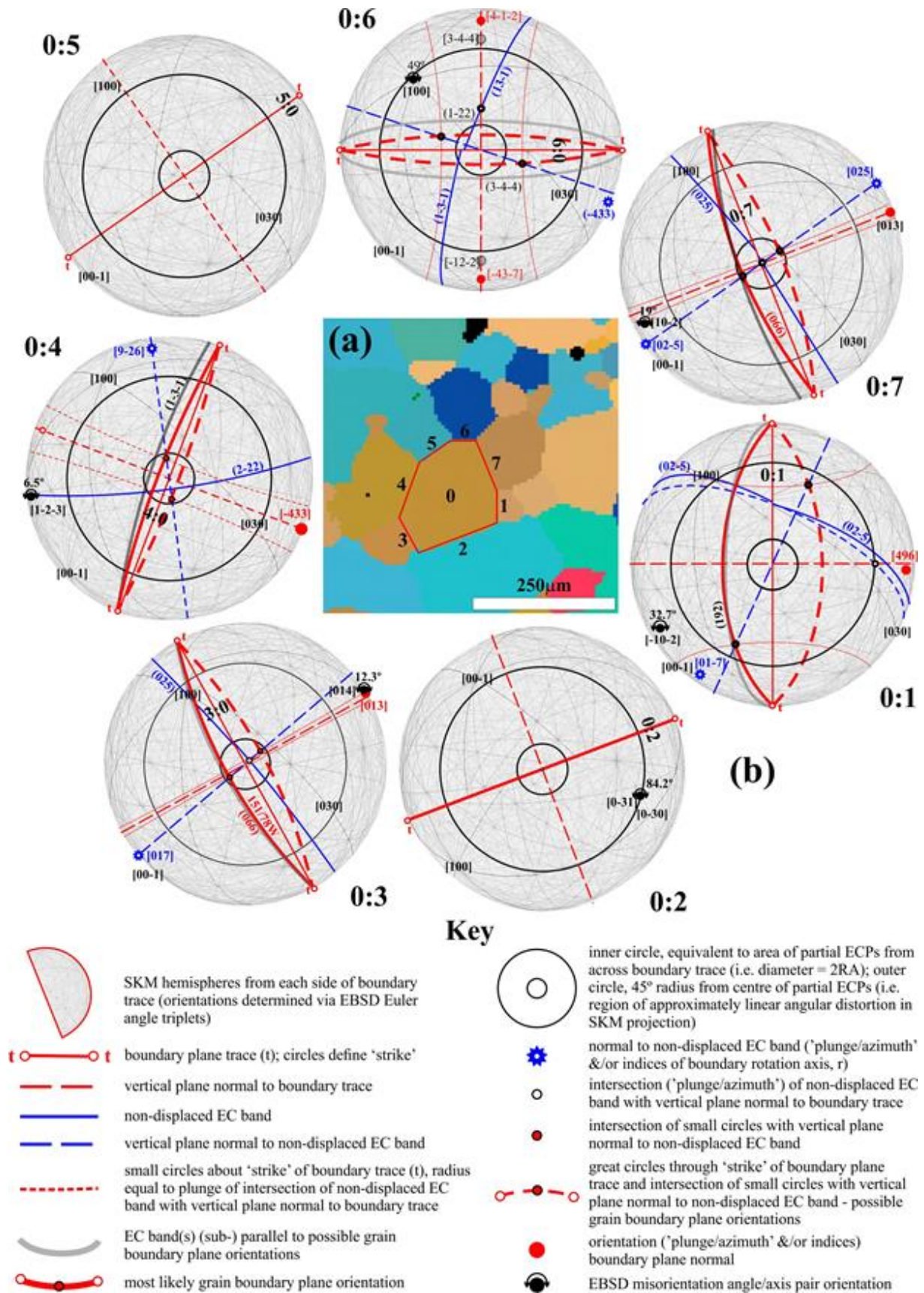


**Figure 11.** Example of potential adaption of method to intergranular boundary orientation determination. (a) EBSD 'all Euler' image of an olivine grain (0) and its immediate neighbours (1-7) from a garnet lherzolite, Thaba Putsoa, Lesotho. (b) SKM 'pairs' from each side of a boundary between grain 0 and grains 1-7; also shown are the elements of the five-parameter boundary method (see key). See Table 3 for a summary of results.

488 Euler angle triplets (Table 3) were measured from adjacent sides of each intragranular boundary  
489 (i.e. between grains 0 and 1, 0 and 2, etc.) and used to define SKM-pairs ‘fitted’ along the trace  
490 orientation of their common boundary (Fig. 11b), in a similar manner to partial-ECPs (e.g. Figs 7, 8  
491 and 10). Note that the triplets and hence SKMs for Grain 0 are effectively constant. The combined  
492 partial-SKMs are then interrogated to identify the relevant relationships (see above) required to  
493 determine the boundary orientation (Fig. 11b). However, due to the increasing distortions that  
494 accrue with distance from the centre of the projection, it is advisable to consider only an  
495 approximately  $45^\circ$  radius small circle region about the centre.

496 Results of the analysis of the olivine intergranular boundary analysis (Fig. 11b) are summarised in  
497 Table 3. Of the seven intergranular boundaries considered, only one (boundary 0:5) provides no  
498 overall solution using the five-parameter method as no lattice plane is continuous across the  
499 boundary trace. Another (boundary 0:2) involves the juxtaposition of opposite hemispheres, again  
500 preventing an overall solution due to the absence of a non-displaced plane. A third (boundary 0:6)  
501 also involves the juxtaposition of opposite hemispheres but now the  $(13\bar{1})$  and  $(\bar{1}3\bar{1})$  planes are  
502 ‘continuous’ across the boundary and hence provide a potential solution but one involving two  
503 possible boundary plane orientations. The validity of this solution depends on whether the  
504 equivalence of different planes of the same family is appropriate in terms of the five-parameter  
505 method. The remaining four boundaries all provide tangible solutions based on the occurrence of  
506 non-displaced lattice planes across the boundary traces. Indeed, three of these boundaries (0:1, 0:3  
507 and 0:7) involve the same non-displaced families of planes and hence rotation axes, specifically  
508  $\{025\}$  and  $\langle 019 \rangle$  respectively. The fourth boundary (0:4) has  $(2\bar{2}2)$  as the non-displaced plane and  
509  $[5\bar{1}3]$  as its rotation axis.

510 Five-parameter analysis indicates that two of the intergranular boundaries (0:3 and 0:7) have the  
511 same orientation (Table 3), parallel to  $(066)$  and with boundary plane normal parallel to  $[037]$ .

512 Interestingly, these boundaries are on opposite sides of the central grain (Fig. 11a). The other two

**Table 3.** Adaption to intergranular boundaries: summary of results (see Figs 11 and 12).

Boundary & Euler angle triplets			Non-displaced EC band	Rotation axis (r)	Rotation angles			Boundary plane (hkl)/[uvw]	TTC	EBSD angle/axis	
					$\omega_r$	$\omega_{\text{tilt}}$	$\omega_{\text{twist}}$				
137.6 102.6 39.5	<b>0:1</b>	147.8 110.8 72.6	(02 $\bar{3}$ )	[01 $\bar{4}$ ]	30.2	27.4	12.7	(192)/[253]	0.06	32.7/[ $\bar{1}0\bar{2}$ ]	
137.0 103.1 39.5	<b>0:2</b>	21.5 135.4 144.0	<i>different hemispheres – no solution</i>								84.2/[0 $\bar{3}1$ ]
137.7 102.8 38.5	<b>0:3</b>	141.9 100.3 50.7	(025)	[019]	12.5	2.5	12.3	(066)/[037]	0.90	12.3/[014]	
137.5 102.6 39.8	<b>0:4</b>	133.9 106.3 34.9	(2 $\bar{2}2$ )	[5 $\bar{1}3$ ]	2.5	1.1	2.2	(1 $\bar{3}1$ )[4 $\bar{3}3$ ]	0.35	6.5/[1 $\bar{2}3$ ]	
137.5 102.7 39.3	<b>0:5</b>	40.8 120.8 129.3	<i>different hemispheres -no solutions</i>								94.2/[221]
137.4 102.7 39.4	<b>0:6</b>	5.3 53.9 114.9	(1 $\bar{3}1$ )	[4 $\bar{3}3$ ]	<i>non-displaced EC band same family but not same plane; also different hemispheres</i>			(1 $\bar{2}2$ )[4 $\bar{2}5$ ]	0.49	49/[100]	
			(1 $\bar{3}1$ )	[4 $\bar{3}3$ ]				(3 $\bar{4}4$ )[5 $\bar{1}4$ ]	0.41		
								(1 $\bar{2}2$ )[4 $\bar{2}5$ ]	0.27		
								(3 $\bar{4}4$ )[5 $\bar{1}4$ ]	0.84		
137.2 103.1 39.4	<b>0:7</b>	133.7 97.8 56.8	(025)	[019]	26.5	5.5	25.8	(066)/[037]	0.90	19.0/[10 $\bar{2}$ ]	
			(02 $\bar{5}$ )	[01 $\bar{9}$ ]				0.68			

513 intergranular boundaries for which solutions have been found (i.e. 0:1 and 0: 4) are parallel to (192)  
514 and (1 $\bar{3}1$ ) planes respectively, with normal directions parallel to [253] and [4 $\bar{3}3$ ], again  
515 respectively.

516 The rotation angles for the intergranular boundaries that provide five-parameter orientation  
517 solutions (Table 3) are derived by translating one of the partial SKMs parallel to the non-displaced  
518 EC/lattice plane until the SKM is reconstituted (Fig. 12). This is the same procedure used for the  
519 partial ECPs (e.g. Figs 7 and 8). The three boundaries sharing a <019> rotation axis exhibit  
520 increasing rotation angles from 12.5° (boundary 0:3), which is only just indicative of an  
521 intergranular boundary, through 26.5° (boundary 0:7) to 30.2° (boundary 0:1). However, according  
522 to their TTC values, boundaries 0:3 and 0:7, which also have the same orientation, are almost pure  
523 twist boundaries, whilst 0:1 is even closer to a pure tilt boundary. The other boundary (0:4) has a  
524 very small rotation angle and is in fact an intragranular boundary, which explains why it provides  
525 the most rigorous five-parameter orientation solution. As none of the boundaries are either pure tilt

526 or pure twist in character, the contributions of the tilt and twist components can also be readily  
 527 determined by simple geometry (Fig. 12 and Table 3).

528 As the Euler angle triplets are known for each side of the seven boundaries (Fig. 11a and Table 3),  
 529 HKL Channle5 software can be used to determine the conventional misorientation angle/axis pair  
 530 for each boundary (Table 3). This approach is based only on the restoration of crystal lattices into

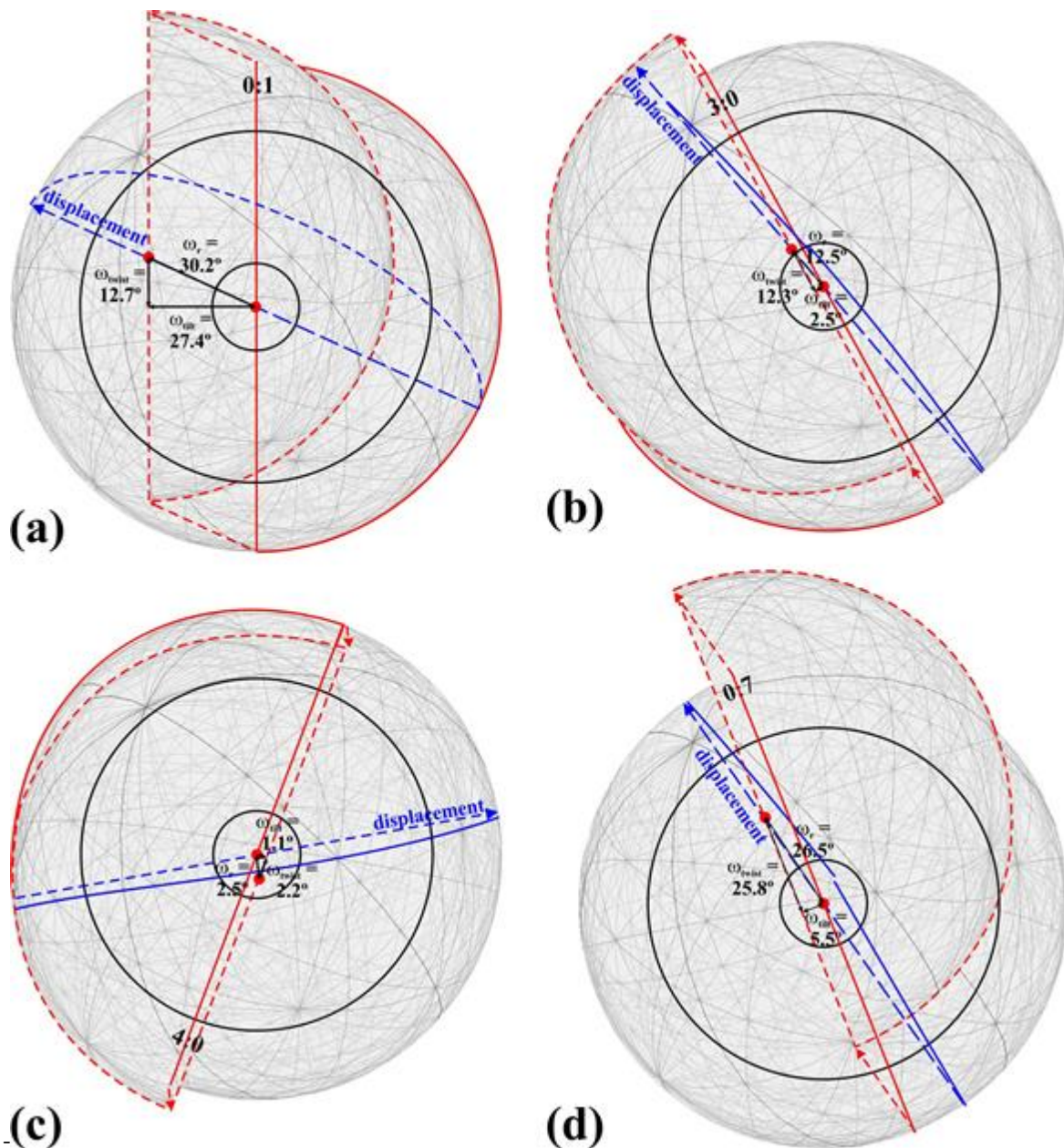


**Figure 12.** Determination of the total and tilt/twist component rotation angles for the four olivine inter/intra-boundaries yielding tangible five-parameter orientation solutions via translation (broken blue arrow) parallel to the non-displaced EC band (solid blue line) of one partial-SKM (broken red outline) relative to its pair until the ‘disrupted’ crystal lattice configuration is restored.

531 parallelism and takes no account of boundary orientation or configuration; thus, all seven  
532 boundaries provide a misorientation angle/axis pair. In contrast, the five-parameter method, can  
533 only provide a rotation angle/axis pair if a solution to the boundary orientation exists; that is  
534 boundaries 0:1, 0:3, 0:4 and 0:7 (see Fig. 12). A direct comparison between the two approaches is  
535 therefore only possible for these four boundaries. In general, comparisons are poor, which is not  
536 surprising as the two measures are fundamentally different. The closest match is for boundary 0:3,  
537 with the five-parameter method giving  $12.5^\circ/[019]$  against  $12.3^\circ/[014]$  for misorientation analysis.  
538 We conclude, as before for intragranular boundaries, that conventional misorientation analysis is  
539 not necessarily a good indicator of complete intergranular boundary relationships.

#### 540 **4.5 Related methods**

541 Having considered how the basic method can be adapted to both EBSD data and intergranular  
542 boundaries, we can now turn to its relationship to existing methods for boundary orientation  
543 determination. Although the method presented here is new *in its entirety*, there are two existing  
544 methods that it does relate to: (1) ‘plane-matching’; and (2) ‘grain boundary character distribution’  
545 (GBCD).

##### 546 *(1) ‘Plane-matching’*

547 The ‘plane-matching’ method (Pumphrey, 1972) recognises that periodic lines observed in  
548 transmission electron microscope images of high angle grain boundaries result from the mismatch  
549 of either low or higher index atom planes across the grain boundary. The common factor in all  
550 observations is that there is at least one set of planes of relatively high atomic density that is either  
551 continuous or only slightly mismatched across the boundary. Watanabe (1983) and Watanabe et al.  
552 (1989) reported ECP observations of grain boundaries that they argued supported the ‘plane-  
553 matching’ model. This led them to suggest that ECP provided a powerful tool for the precise  
554 determination of crystallographic orientations; for example, to determine the relative orientation  
555 relationship between adjacent grains that geometrically characterise a grain boundary. In terms of

556 the present model, ‘plane-matching’ is equivalent to the non-displaced diffraction band. However,  
 557 the ‘plane-matching’ approach does not determine the orientation of the grain boundary; rather, it  
 558 constrains the direction of growth of one grain at the expense of another grain (e.g. during  
 559 recrystallisation). Nevertheless, as Watanabe (1983) and Watanabe et al. (1989) provided the ECPs  
 560 for the boundaries they investigated, it seems apposite to consider examples in terms of the present  
 561 model, particularly as the ‘plane-matching’ approach did not define the boundary orientations.

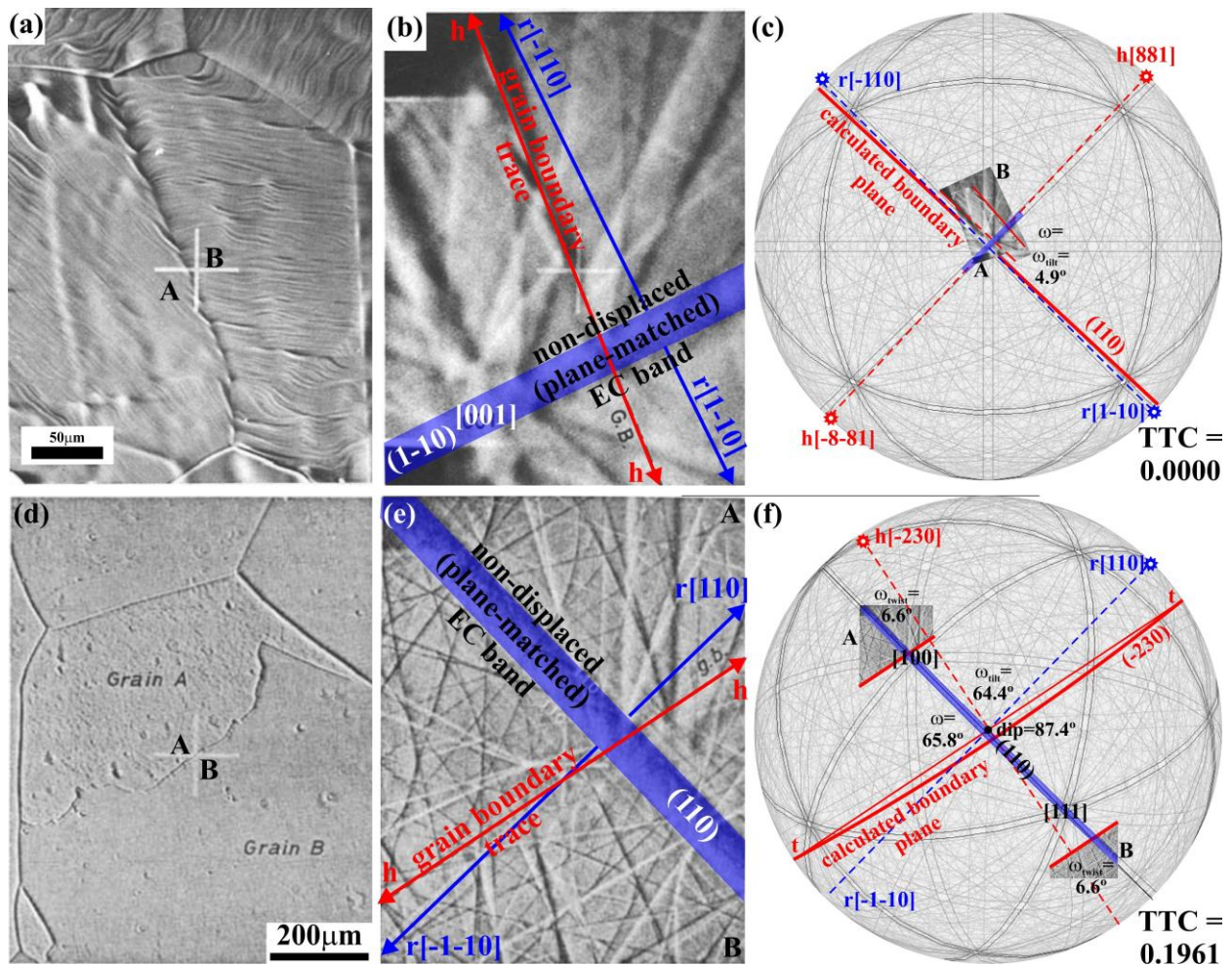


**Figure 13.** Comparisons between the current and ‘plane-matching’ methods: (a) – (c) low-angle (intragranular) boundary between two grains (A, B) in bcc Fe-6.5 mass% Si alloy (Watanabe et al., 1989, Fig. 4); (d) – (f) high-angle grain boundary between two grains (A, B) in bcc Fe-3% Si alloy (Watanabe, 1983, Fig. 1). Colour coding and nomenclature/symbols as for Figs 3, 5, 7, 8 and 10-12. (a) and (d) SEM images of boundary microstructures (cross indicates beam incident position). (b) and (e) Partial ECPs from the beam incidence positions. (e) Interpretation of the low-angle (intragranular) boundary via the current method as a vertical pure tilt boundary (TTC = 0) parallel to (110) with 4.9° misorientation. (f) Interpretation of the high-angle grain boundary via the current method as a sub-vertical (87.4° dip) general boundary (TTC = 0.20) parallel to  $(\bar{2}30)$  with 65.8° misorientation comprising 64.4° tilt and 6.6° twist components.

562 The first example is a low-angle (intragranular) boundary between two grains in bcc Fe-6.5 mass%  
563 Si alloy (Watanabe et al., 1989, Fig. 4; see Fig. 13a). Partial ECPs from across the boundary (Fig.  
564 13b) clearly reveal the matched plane as (1-10), which is also the non-displaced EC band.  
565 Superposing the partial ECPs onto a SKM for bcc iron (Fig. 13c) indicates that the matched  
566 plane/non-displaced EC band passes through the projection centre; the band must therefore be  
567 vertical and hence the rotation axis is horizontal, parallel to  $[\bar{1}10]/[1\bar{1}0]$ . Furthermore, not only  
568 does the boundary trace also pass through the projection centre but it is almost coincident with the  
569 vertical normal to the matched plane/ non-displaced EC band. Applying the method described in  
570 this contribution constrains the boundary plane to be vertical (Fig. 13c); however, the very slight  
571 off-set between boundary trace and non-displaced EC band means that the boundary plane normal  
572 direction is parallel to  $[881]/[\bar{8}\bar{8}1]$ . Combining these directions with the rotation axes via the Excel  
573 spreadsheet in the Appendix yields a TCC value of zero; thus this is a pure tilt boundary. Finally,  
574 using the internal scaling present in the ECPs and SKM (Fig. 13c) allows the tilt angle to be  
575 determined as  $4.9^\circ$ , confirming this as a low-angle (intragranular) boundary.

576 The second example is a high-angle grain boundary between two grains in bcc Fe-3% Si alloy  
577 (Watanabe, 1983, Fig. 4; see Fig. 13d). Partial ECPs from across the boundary (Fig. 13e) reveal the  
578 matched plane and hence non-displaced EC band to be (110). Superposing the partial ECPs onto a  
579 SKM for bcc iron (Fig. 13f) indicates that the matched plane/non-displaced EC band does not quite  
580 pass through the projection centre; the band therefore is not quite vertical and hence the rotation  
581 axis is sub-horizontal parallel to  $[110]$ . Whilst the boundary trace almost passes through the  
582 projection centre, it is clearly not parallel to the matched plane/non-displaced EC band. Applying  
583 the method described in this contribution constrains the boundary plane to be parallel to  $(\bar{2}30)$  and  
584 to dip at  $84.7^\circ$ , with the boundary plane normal direction constrained to be parallel to  $[\bar{2}30]$  (Fig.  
585 13f). Combining these directions with the rotation axes via the Excel spreadsheet in the Appendix  
586 yields a TCC value of 0.20, indicating a general boundary albeit with a dominant tilt component.  
587 Using the internal scaling present in the ECPs and SKM (Fig. 13f) allows not only the total

588 boundary misorientation to be determined at  $65.8^\circ$  but also the tilt and twist components at  $64.4^\circ$   
589 and  $6.6^\circ$  respectively. The fact that such a large grain boundary misorientation can still exhibit a  
590 matched plane/non-displaced EC band suggests that the two adjacent grains share an affinity (see  
591 Watanabe et al., 1989).

## 592 (2) *GBCD*

593 In principal, the GBCD method (e.g. Watanabe, 1979, 1984, 1986 and 1988; Watanabe et al., 1981  
594 and 1986) should have much in common with our method as it targets the five parameters needed to  
595 define the complete orientation of a boundary. However, in practice there are significant differences  
596 between the two approaches. GBCD concerns the description of the type and frequency of grain  
597 boundaries in polycrystalline materials. In particular, it seeks to characterise the distribution of  
598 special types of boundaries that might impact upon material properties and behaviours. The grain-  
599 boundary distribution is expressed in terms of the conventional five parameters from measurements  
600 of grain orientations and the orientations of the lines formed where grain boundaries intersect the  
601 plane of observation. The fundamental aim of GBCD is to provide a quantitative description of the  
602 amount and type of (special) boundaries that are present in a polycrystalline material (e.g. CSLs).

603 A significant advantage that the GBCD approach has over the method presented here is that it has  
604 been automated via EBSD and stereology (e.g. Saylor and Rohrer, 2002; Saylor et al., 2004; Rohrer  
605 et al., 2004b; Marquardt et al., 2015; Marquardt & Faul, 2018) and hence can consider large  
606 populations of boundaries that potentially provide statistically significant observations. However,  
607 the method does have disadvantages. In particular, it requires either 3D EBSD data derived via  
608 serial sectioning or 2D EBSD data from samples lacking CPO to ensure the approximately random  
609 distribution required for stereological determination of grain boundary normal directions (Randle  
610 and Davies 2001; Rohrer 2007 and 2011; Brandon 2010; Marquardt et al., 2015). In addition,  
611 GBCD relies on the three disorientation parameters to define the minimum misorientation  
612 angle/axis pair, which we have suggested is independent of boundary orientation except in special

613 circumstances. Further comparison between GBCD and the method described here is beyond the  
614 scope of this contribution.

#### 615 **4.6 Accuracy, precision and error**

616 The method introduced here is overtly manual and practical, even when involving Euler angle  
617 triplets determined via EBSD. It is therefore subject to the accuracy, precision and error limitations  
618 inherent in such approaches, particularly in terms of visual inspection/interpretation and manual  
619 measurements. In general, errors depend on the resolution and quality of the diffraction patterns  
620 (either EC or EBSD), the size of the spherical region, boundary inclination and the precision of the  
621 stereographic projection, amongst other factors. As such, it is difficult if not impossible to derive  
622 precise relative error(s) or error function(s). Nevertheless, the original potential error from which all  
623 others ultimately derive is in the recognition of the non-displaced diffraction band and the  
624 associated linear and/or angular measurements (misorientation displacements and/or angles). If the  
625 non-displaced band is clearly defined and particularly if it is located within  $\sim 45^\circ$  of the centre of  
626 projection, then measurements should be both accurate and precise. However, if the non-displaced  
627 band is poorly defined, which tends to be exacerbated if it occurs towards the periphery of the  
628 projection, then accuracy and indeed precision are impacted. In general, the best possible accuracy  
629 is probably to within one decimal place for both angular and linear measurements. In terms of  
630 actual boundary orientations, this means that steeper boundaries are likely to be more accurately  
631 defined than shallower boundaries.

632 Whilst the accuracy and precision in locating the boundary trace are typically high, the recognition  
633 of the actual boundary plane depends on stereographic projection. The projection involves plotting  
634 the non-displaced diffraction band and its vertical normal plane, as well as the boundary trace and  
635 normal. Initial errors in defining the non-displaced diffraction band can therefore be propagated. In  
636 general, the orientation of the boundary trace can be defined accurately for straight boundaries;  
637 however, curved boundaries need to be considered as linear segments, which must introduce some

638 error or approximation. In addition, magnification of boundary images and especially EBSD-  
639 derived ‘maps’ can also introduce pixilation of boundary traces, leading to lack of precision and  
640 error. The stereographic solution also provides two alternative boundary orientations, with the final  
641 choice depending on the presence/absence of a coincident (low-index) lattice plane, which may not  
642 be perfectly matched and hence could add additional error.

643 The method presented is based on the assumption that intragranular boundaries are constrained to  
644 low-index crystal lattice planes (i.e. the conventional Read-Shockley model), which can introduce  
645 limitations in solutions for boundary plane orientation and hence errors. Whilst the basic  
646 assumption can be geometrically established based on dislocation systems that usually operate with  
647 short Burger vectors, more general intragranular low angle or composite boundaries (e.g. those with  
648 orientation gradients that can be solved for combinations of different slip systems) can deviate from  
649 the conventional approach. Whilst this situation must be recognised, we would emphasise that  
650 although the basic premise of the method is the Read-Shockley model, the solutions derived are not  
651 necessarily low-index planes or directions (e.g. Tables 1-3). Indeed, the converse question can be  
652 posed as to how valid is the practice of ‘rounding’ the indices to the nearest low angle solution.

#### 653 **4.7 Future developments**

654 This contribution has focussed on deriving a practical method to determine the complete (five-  
655 parameter) orientation of intragranular boundaries. Whilst such a method has been demonstrated, it  
656 certainly needs further testing via more examples, case studies and applications. These aspects  
657 represent current work in progress. In addition, as presented the method is overtly practical and  
658 hence applicable to relatively small datasets; it does not compare therefore with the opportunities  
659 provided by EBSD misorientation analysis, although as demonstrated such analysis may contain  
660 ambiguity in terms of boundary plane orientation. Nevertheless, the practical five-parameter  
661 boundary orientation method would certainly benefit from both quantification and automation. The  
662 former is also currently being investigated via several approaches involving definition of the

663 orientation matrix ( $g$ ) in terms of crystal indices, Euler angle triplets and quaternions, although the  
664 plunge and azimuth of the boundary plane normal still have to be determined using the method  
665 proposed here. The latter requires (image) recognition of boundary traces and comparison of  
666 (quantitative) Euler angle triplet based orientations for adjacent regions across boundaries to define  
667 the necessary parameters. Hopefully, should the basic practical method prove viable, full  
668 quantification and automation will follow.

669

## 5. CONCLUSIONS

670 Boundaries are important features of polycrystalline materials and influence most properties,  
671 characteristics and behaviours. Accurate, reproducible and ideally rapid and efficient definition of  
672 boundary configuration is central therefore to furthering understanding polycrystalline materials.  
673 The complete definition of boundary orientation involves the misorientation between the crystal  
674 lattices of adjacent regions across the boundary and also the physical attitude of the boundary plane  
675 (e.g. the direction of the plane normal). Whilst it has become relatively easy and efficient to  
676 determine boundary misorientation (e.g. via EBSD in the SEM), definition of the boundary plane  
677 orientation has proved difficult.

678 This contribution has presented a practical method to determine the complete ‘five-parameter’  
679 orientation of intragranular boundaries based on matching the spherical geometries of ‘partial’ SEM  
680 electron channelling patterns (ECPs) across boundary traces. The method assumes that intragranular  
681 boundaries are constrained to low-index crystal lattice planes (i.e. Read-Shockley model) and relies  
682 on recognising electron channelling bands, equivalent to crystal lattice planes, which are not  
683 displaced across or are parallel to the boundary trace. The former indicates the translation or  
684 displacement direction of one side of the boundary relative to the other, such that its normal  
685 direction defines the boundary rotation axis. Stereographic projection considerations of the  
686 spherical geometry relationships between the non-displaced channelling band and the boundary  
687 trace, together with the boundary trace parallel channelling bands, allow for determination of the

688 orientation of the boundary plane. Finally, one partial pattern is translated relative to the other  
689 parallel to the non-displaced channelling band until the undistorted ECP is restored, from which the  
690 boundary rotation angle can be measured.

691 Although developed from EC theory for intragranular boundaries, it has been shown how the  
692 method can be adapted relatively simply to both EBSD data (i.e. Euler angle triplets), involving the  
693 use of interactive spherical Kikuchi maps, and intergranular boundaries. However, not all  
694 intergranular boundaries may possess the necessary relationships between adjacent grains. In  
695 addition, the new method not only readily distinguishes between tilt and twist boundaries but also  
696 allows the relative contributions of these two end-member forms to the statistically more common  
697 general boundary configurations to be accurately determined and represented, both in terms of  
698 component rotation angles and also the tilt-twist component (TTC) index.

699 Whilst this contribution is principally concerned with the derivation of a basic method to determine  
700 accurately the complete five-parameter orientation of intra- and some inter- granular boundaries, the  
701 examples included suggest that conventional (i.e. EBSD) misorientation analysis may not  
702 necessarily provide an accurate and/or reliable representation of (intragranular) boundary  
703 configurations. Misorientation analysis is based only on matching crystal lattices via rotations about  
704 a specific axis (i.e. angle/axis pairs) and is independent of boundary configuration. We anticipate  
705 therefore that our method could potentially offer a new field of analysis based on data that are  
706 readily available and stimulate discussions on the nature and significance of (intragranular)  
707 boundaries.

708 **Acknowledgements-** This paper is dedicated to the memory of Professor Adolphe Nicolas for his  
709 seminal contributions to Earth Sciences in general and to the understanding of microstructural  
710 processes in particular. We thank Andrew Walker for numerous discussions on the methods  
711 involved. GEL also thanks Dave Mainprice for many years of discussions on all aspects of  
712 misorientation. ALL was funded by a University of Leeds teaching award and University of Tromsø

713 postdoctoral fellowship. MK was supported by a postdoctoral research fellowship of the Iceland  
714 Research Fund (Rannís 152726-051) and a Deutsche Forschungsgemeinschaft (DFG KA 3532/2-1)  
715 standard grant. We are grateful for the help and advice offered by the Journal's editors, Philippe  
716 Agard and Andrea Tommasi, and for the detailed and often perceptive comments of two anonymous  
717 reviewers, all of which contributed to the final version of this paper.

## 718 REFERENCES

- 719 Allsopp, H., Bristow, J.W., Smith, C.B., Brown, R., Gleadow, A.J.W., Kramers, J.D. and Garvic, O.  
720 1989. A summary of radiometric dating methods applicable to kimberlites and related rocks. In:  
721 Ross, J.L. (Ed.), *Kimberlites and Related Rocks: Their Composition, Occurrence, Origin and*  
722 *Emplacement*. Blackwell, Oxford, 349–357.
- 723 Amouyal, Y.; Rabkin, E.; Mishin, Y. 2005. Correlation between grain boundary energy and  
724 geometry in Ni-rich NiAl. *Acta Materialia* **53**, 3795–3805.
- 725 Bachmann, F., Hielscher, R. and Schaeben, H. 2010. Texture analysis with MTEX—free and open  
726 source software toolbox. *Solid State Phenomena* **160**, 63–68.
- 727 Boisen, M.B. and Gibbs G.V. 1990. Mathematical Crystallography. *Reviews in Mineralogy* **15**,  
728 Mineralogical Society of America, 7276.
- 729 Bond, W.L. 1976. *Crystal Technology*, John Wiley & Son.
- 730 Bragg, W. L. 1940. Discussion. Part I. *Proceedings of the Physical Society* **52**, 54-56.
- 731 Brandon. D. 2010. 25 Year perspective defining grain boundaries: an historical perspective: The  
732 development and limitations of coincident site lattice models. *Materials Sciences Technology* **26**,  
733 762–773. doi:10.1179/026708310X12635619987989
- 734 Buranova, Y., Rosner, H., Divinski, S.V., Imlau, R. and Wilde, G. 2016. Quantitative  
735 measurements of grain boundary excess volume from HAADF-STEM micrographs. *Acta*  
736 *Materialia* **106**, 367-373.
- 737 Burgers, J. M. 1939a. Some considerations on the fields of stress connected with dislocations in a  
738 regular crystal lattice I. *Proceedings of the Koninklijke Nederlandse Akademie van*

- 739 *Wetenschappen* 42, 293-325.
- 740 Burgers, J. M. 1939b. Some considerations on the fields of stress connected with dislocations in a  
741 regular crystal lattice II (Solutions of the equations of elasticity for a non-isotropic substance of  
742 regular crystalline symmetry). *Proceedings of the Koninklijke Nederlandse Akademie van*  
743 *Wetenschappen* 42, 378-399.
- 744 Burgers, J. M. 1940. Geometrical considerations concerning the structural irregularities to be  
745 assumed in a crystal: *Proceedings of the Physical Society* 52, 23-33
- 746 Cross, I. and Randle, R. 2003. Lowest angle solution versus low-index axis solution for  
747 misorientations. *Scripta Materialia* **48**, 1587–1591.
- 748 Dash, M.K., Karthikeyan, T. and Saroja, S. 2017. Five-parameter grain boundary determination in  
749 annealed ferrite structure using electron backscatter diffraction and serial sectioning technique.  
750 *Transactions of the Indian Institute of Metallurgy* **70**,133–143.  
751 DOI 10.1007/s12666-016-0868-x
- 752 Day, A.P. 2008. Spherical EBSD. *Journal of Microscopy* 230, 472-486.  
753 <https://doi.org/10.1111/j.1365-2818.2008.02011.x>
- 754 Day, A.P. 2009. Spherical Kikuchi maps and other rarities. In, Schwartz, A.J., Kumar, M., Adams,  
755 B.L. and Field, D.P., *Electron Backscatter Diffraction in Materials Science*. Springer Nature  
756 Switzerland AG.
- 757 Dingley, D.J. 1989. Developments in on-line crystal orientation determination. *Institute of Physics*  
758 *Conference Series* **98**, 473–476.
- 759 Friedel, G. 1913. Sur les symétries cristallines que peut révéler la diffraction des rayons X. C.R.  
760 Acad. Sci. Paris 157, 1533-1536.
- 761 Goldstein, J.I. and Yakowitz, H. 1975. *Practical Scanning Electron Microscopy*. Plenum, New  
762 York.
- 763 Gourdet, S., Jonas, J.J and Montheillet, E. 1998. Minimum-angle versus low-index axis rotations  
764 for representing small- and large-angle grain boundary misorientations in cubic lattices. *Journal*

- 765 *of Applied Crystallography* **31**, 204-211.
- 766 Grimmer, H., Bollmann, W. and Warrington, D. H. 1974. Coincidence-site lattices and complete  
767 pattern-shift in cubic crystals. *Acta Crystallographica* **A30**, 197–207.  
768 doi:10.1107/S056773947400043X
- 769 Handscomb D.C. 1957. On the random disorientation of two cubes. *Canadian Journal of*  
770 *Mathematics* **10**, 85-.
- 771 Hielscher, R., Bartel, F. and Britton, T.B. 2019. Gazing at crystal balls: Electron backscatter  
772 diffraction pattern analysis and cross correlation on the sphere. *Ultramicroscopy* 207,112836.
- 773 Hirsch, P.B., Howie, A. and Whelan, M.J. 1962. On the production of X-rays in thin metal foils.  
774 *Philosophical Magazine* **7**, 2095-2100.
- 775 Jhang, J.W., Jain, T., Lin, H.K. and Lan, C. W. 2018. Possible twinning operations during  
776 directional solidification of multi-crystalline silicon. *Crystal Growth and Design* 18, 2518-2524.
- 777 Joy, D.C. 1974. Electron channelling patterns in the SEM. In, Holt, D. B., Muir, M. D., Grant, P. R.  
778 and Boswarva, I. M. (eds) *Quantitative Scanning Electron Microscopy*. Academic, London, 131-  
779 82.
- 780 Joy D.C., Newbury, D.C. and Davidson, D.L. 1982. Electron channelling patterns in the scanning  
781 electron microscope. *Journal of Applied Physics* **53**, R81-122. <https://doi.org/10.1063/1.331668>
- 782 Kim, C-S., Hu, Y., Rohrer, G.S. and Randle, V. 2005. Five-parameter grain boundary distribution  
783 in grain boundary engineered brass. *Scripta Materialia* **52**, 633–637
- 784 Langdon, T.G. 2006. Grain boundary sliding revisited: Developments in sliding over four decades.  
785 *Journal of Materials Science* 41, 597–609.
- 786 Lisle, R.J. and Walker, R.J. 2013. The estimation of fault slip from map data: The separation-pitch  
787 diagram. *Tectonophysics* 583, 158–163.
- 788 Lloyd, G.E. 1987. Atomic number and crystallographic contrast images with the SEM: a review of  
789 backscattered electron techniques. *Mineralogical Magazine* **51**, 3-19.
- 790 Lloyd, G.E., Farmer, A.B. and Mainprice, D. 1997. Misorientation analysis and the formation and

- 791 orientation of subgrain and grain boundaries. *Tectonophysics* 279, 55-78.
- 792 Lloyd, G.E. and Ferguson, C.C. 1986. A spherical electron-channelling pattern map for use in  
793 quartz petrofabric analysis. *Journal of Structural Geology* 8, 517–526.
- 794 Mackenzie, J.K. 1958. Second paper on statistics associated with the random disorientation of  
795 cubes. *Biometrika* **45**, 229-240.
- 796 Mackenzie, J.K. and Thomson, M.J. 1957. Some statistics associated with the random disorientation  
797 of cubes. *Biometrika* **44**, 205-210.
- 798 Marquardt, K. and Faul, U.H. 2018. The structure and composition of olivine grain boundaries: 40  
799 years of studies, status and current developments. *Physics and Chemistry of Minerals* **45**, 139–  
800 172. <https://doi.org/10.1007/s00269-017-0935-9>
- 801 Marquardt K., Rohrer G. S., Morales L., Rybacki E., Marquardt H. and Lin B. 2015. The most  
802 frequent interfaces in olivine aggregates: the GBCD and its importance for grain boundary  
803 related processes. *Contributions to Mineralogy and Petrology* **170**, 40-57.  
804 <https://doi.org/10.1007/s00410-015-1193-9>
- 805 Mainprice, D., Lloyd, G.E. and Casey, M. 1993. Individual orientation measurements in quartz  
806 polycrystals - advantages and limitations for texture and petrophysical property determinations.  
807 *Journal of Structural Geology* 15, 1169-1187.
- 808 Mercier, J.-C. and Carter, N.L. 1985. Pyroxene geotherms. *Journal of Geophysical Research* 80,  
809 3349–3362. <https://doi.org/10.1029/JB080i023p03349>.
- 810 Mohamed, F.A. 2011. Micrograin Superplasticity: Characteristics and Utilization. *Materials* **4**,  
811 1194-1223; doi:10.3390/ma4071194
- 812 Nieto-Fuentes, R., Nieto-Samaniego, Á.F., Xu, S.-S. and Alaniz-Álvarez, S.A. 2014. Software for  
813 determining the true displacement of faults. *Computers and Geosciences* 64, 35–40.
- 814 Nixon, P.H. and Boyd, F.R. 1973. Petrogenesis of the granular and sheared ultrabasic nodule suite  
815 in kimberlites. In: Nixon, P.H. (Ed.), *Lesotho Kimberlites*. Cape and Transvaal Printers, 48–56.
- 816 Prior, D.J., Boyle, A.P., Brenker, F., Cheadle, M.C., Day, A., Lopez, G., Peruzzo, L., Potts, G.J.,

- 817 Reddy, S., Spiess, R., Timms, N.E., Trimby, P., Wheeler, J., Zetterström, L., 1999. The  
818 application of electron backscatter diffraction and orientation contrast imaging in the SEM to  
819 textural problems in rocks. *American Mineralogist* **84**, 1741–1759. [http://dx.doi.org/10.2138/am-](http://dx.doi.org/10.2138/am-1999-11-1204)  
820 [1999-11-1204](http://dx.doi.org/10.2138/am-1999-11-1204).
- 821 Prior, D.J., Mariani, E., Wheeler, J., 2009. EBSD in the Earth Sciences: applications, common  
822 practice, and challenges. In: Schwartz, A., Kumar, M., Adams, B., Field, D. (Eds.), *Electron*  
823 *Backscatter Diffraction in Materials Science*. Springer, Boston, MA, pp. 345–360.  
824 [http://dx.doi.org/10.1007/978-0-387-88136-2\\_26](http://dx.doi.org/10.1007/978-0-387-88136-2_26).
- 825 Pumphrey, P.H. 1972. A plane matching theory of high angle grain boundary structure. *Scripta*  
826 *Metallurgica* **6**, 107-114.
- 827 Randle, V. 1993. *The Measurement of Grain Boundary Geometry*. Institute of Physics Publications,  
828 Bristol.
- 829 Randle, V. 2003. *Microtexture Determination and its Application*, 2nd edn. Maney Press, London.
- 830 Randle, V. 2006. ‘Five-parameter’ analysis of grain boundary networks by electron backscatter  
831 diffraction. *Journal of Microscopy* **222**, 69–75
- 832 Randle, V. and Davies, H. 2001. A comparison between three-dimensional and two-dimensional  
833 grain boundary plane analysis. *Ultramicroscopy* **90**, 153–162.
- 834 Read, W.T. and Shockley, W. 1950. Dislocation models of crystal grain boundaries. *Physical*  
835 *Review* **78**, 275-289.
- 836 Redmond, J.L. 1972. Null combination in fault interpretation. *American Association of Petroleum*  
837 *Geologists Bulletin* **56**, 150-166.
- 838 Rohrer, G.S. 2007. The distribution of grain boundary planes in polycrystals. *Journal of the*  
839 *Minerals Metals and Materials Society* **59**, 38–42.
- 840 Rohrer, G.S. 2011. Grain boundary energy anisotropy: a review. *Journal of Material Science* **46**,  
841 5881–5895. DOI 10.1007/s10853-011-5677-3.
- 842 Rohrer, G.S. and Randle, V. 2009. Measurement of the five parameter grain boundary distribution

- 843 from planar sections. In, Schwartz, A.J., Kumar, M., Adams, B.L. and Field, D.P., Electron  
844 Backscatter Diffraction in Materials Science. Springer.
- 845 Rohrer, G.S., Saylor, D.M., El Dasher, B., Adams, B.L., Rollett, A.D. and Wynblatt, P. 2004. The  
846 distribution of internal interfaces in polycrystals. *Zeitschrift Für Metallkunde* **95**,197–214. doi:  
847 10.3139/146.017934
- 848 Saylor, D.M. and Rohrer, G.S. 2002. Determining crystal habits from observations of planar  
849 sections. *Journal of the American Ceramics Society* **804**, 2799–2804.
- 850 Saylor, D.M., El Dasher, B.S., Adams, B.L. and Rohrer, G.S. 2004. Measuring the five-parameter  
851 grain-boundary distribution from observations of planar sections. *Metallurgical and Materials*  
852 *Transactions A* **35**, 1981–1989.
- 853 Shockley, W. and Read, W.T. 1949. Quantitative predictions from dislocation models of crystal  
854 grain boundaries. *Physical Review* **75**, 692-692.
- 855 Sutton, A.P. and Balluffi, R.W. 1995. *Interfaces in crystalline materials*. Oxford, UK: Oxford  
856 University Press.
- 857 Sutton, A.P., Banks, E.P. and Warwick, A.R. 2015. The five-dimensional parameter space of grain  
858 boundaries. *Proceedings of the Royal Society A* **471**, Article Number: 20150442.  
859 <http://dx.doi.org/10.1098/rspa.2015.0442>
- 860 Venables, J.A. and Harland, C.J. 1973. Electron backscattering patterns - a new technique for  
861 obtaining crystallographic information in the scanning electron microscope. *Philosophical*  
862 *Magazine* **27**, 1193-1200.
- 863 Wallis, D., Hansen, L.N., Tasaka, M., Kumamoto, K.M., Parsons, A.J., Lloyd, G.E., Kohlstedt,  
864 D/L. and Wilkinson, A.J. 2019. The impact of water on slip system activity in olivine and the  
865 formation of bimodal crystallographic preferred orientations. *Earth and Planetary Science*  
866 *Letters* **508**, 51–61. <https://doi.org/10.1016/j.epsl.2018.12.007>
- 867 Warrington, D. H. and Boon, M. 1975. Ordered structures in random grain boundaries; some  
868 geometrical probabilities. *Acta Metallurgica* **23**, 599-607.

- 869 Warrington, D.H. and Bufalini, P. 1971. The coincidence site lattice and grain boundaries. *Scripta*  
870 *Metallurgica* **5**, 771-776.
- 871 Watanabe, T. 1979. Misorientation dependence of grain boundary sliding in 1010 tilt zinc bi-  
872 crystals. *Philosophical Magazine, Physics of Condensed Matter, Defects and Mechanical*  
873 *Properties* **40**, 667–683.
- 874 Watanabe, T. 1983. Observations of plane-matching grain boundaries by electron channelling  
875 patterns. *Philosophical Magazine* **A47**, 141-146. <https://doi.org/10.1080/01418618308243114>
- 876 Watanabe, T. 1984. An approach to grain-boundary design for strong and ductile polycrystals. *Res*  
877 *Mechanica* **11**, 47-84.
- 878 Watanabe, T. 1986. Grain boundary design for new materials. In: *Grain Boundary Structure and*  
879 *Related Phenomena*. Proceedings of JIMIS-4 (1986), Supplement to Transactions of the Japan  
880 Institute of Metals, 73-82.
- 881 Watanabe, T. 1988. Grain-boundary design for desirable mechanical properties. *Journal de*  
882 *Physique* **19**, 507-519.
- 883 Watanabe, T., Fujii, H., Oikawa, H. and Arai, K.I. 1989. Grain boundaries in rapidly solidified and  
884 annealed Fe-6.5 mass% Si polycrystalline ribbons with high ductility. *Acta Metallurgica* **37**,  
885 941-952.
- 886 Watanabe, T., Kawamata, Y. and Karashima, S. 1986. Grain boundary character distributions for  
887 recrystallization structures in Fe-3% Si. In: *Grain Boundary Structure and Related Phenomena:*  
888 *Proceedings of JIMIS-4 (1986), Supplement to Trans. of the Japan Institute of Metals*, pp. 601-  
889 607.
- 890 Watanabe, T., Yoshikawa, N., and Karashima, S. 1981. Grain boundary character distributions in  
891 recrystallisation structures of deformed aluminium single crystals. In: *Proceedings of the Sixth*  
892 *International Conference on Textures of Materials (ICOTOM-6)*, Vol. 1, Japanese Iron and Steel  
893 Institute, Japan, 609-618.
- 894 Wheeler J, Prior D.J., Jiang Z., Spiess R., and Trimby P.W. 2001. The petrological significance of

- 895 misorientations between grains. *Contributions to Mineralogy and Petrology* 141.109–124.
- 896 Wheeler, J., Mariani, E., Piazzolo, S., Prior, D.J., Trimby, P. and Drury, M.R. 2009. The weighted  
897 Burgers vector: a new quantity for constraining dislocation densities and types using electron  
898 backscatter diffraction on 2D sections through crystalline materials. *Journal of Microscopy* **233**,  
899 482–494.
- 900 Wieser, P.E. Edmonds, M., Maclennan, J. and Wheeler, J. 2020. Microstructural constraints on  
901 magmatic mushes under Kīlauea Volcano, Hawai‘i. *Nature Communications* **11**, 1-14 |  
902 <https://doi.org/10.1038/s41467-019-13635-y>
- 903 Xu, S.-S., Velasquillo-Martinez, L.G., Grajales-Nishimura, J.M., Murillo-Muneto, G. and Nieto-  
904 Samaniego, A.F. 2007. Methods for quantitatively determining fault slip using fault separation.  
905 *Journal of Structural Geology* 29, 1709-1720.
- 906 Xu, S.-S., Nieto-Samaniego, A.F. and Alaniz-Álvarez, S.A. 2009. Quantification of true  
907 displacement using apparent displacement along an arbitrary line on a fault plane.  
908 *Tectonophysics* 467, 107–118.
- 909 Yamada, E. and Sakaguchi, K. 1995. Fault-slip calculation from separations. *Journal of Structural*  
910 *Geology* 17, 1065-1070.
- 911 Zaefferer, S. and Elhami, N., 2014. Theory and application of electron channelling contrast imaging  
912 1288 under controlled diffraction conditions. *Acta Materialia* **75**, 20-50.  
913 <https://doi.org/10.1016/j.actamat.2014.04.018>
- 914 Zhu, C., Kaufmann, K. and Vecchio, K. 2019. Automated reconstruction of spherical Kikuchi maps.  
915 *Microscopy and Microanalysis* 25, 912-923. DOI: <https://doi.org/10.1017/S1431927619000710>  
916

917

**APPENDIX:**

918 **Excel spreadsheet to assist crystallographic calculations involved in the five-parameter based**  
 919 **determination of the orientation of intragranular boundaries**

920 We have developed a simple Excel spreadsheet to perform the crystallographic calculations  
 921 involved in the five-parameter based determination of the orientation of intragranular boundaries  
 922 (see below). This Appendix explains the calculations, which are all standard crystallography  
 923 relationships; all user input cells are indicated by bold red text. In general, the determination of the  
 924 five-parameters involves crystal directions,  $[uvw]$ , rather than planes,  $(hkl)$ . The description is based  
 925 on olivine; modifications for other phases and in particular crystal symmetries are indicated where  
 926 necessary. Note that the calculations involve rounding, whilst some indices can be user-simplified.

927 **0. Miller/Miller-Bravais conversions (hexagonal and trigonal lattices)**

928 As the crystal operations involved in boundary determination assume Miller indices and notation  
 929 (i.e.  $(hkl)$  or  $[uvw]$ ), it is necessary to convert between these and Miller-Bravais indices applicable  
 930 to hexagonal and trigonal lattices (i.e.  $(HKIL)$  or  $[UVTW]$ ).

931 *Miller-Bravais to Miller*

932 Directions:  $u = U - T$        $v = V - T$        $w = W$       (A1a)

933 Planes:  $h = H$        $k = K$        $l = L$       (A1b)

934 *Miller to Miller-Bravais*

935 Directions:  $U = (2u - v)/3$        $V = (2v - u)/3$        $T = (u + v)/3$        $W = w$  (A1c)

936 Planes:  $H = h$        $K = k$        $I = h + k$        $L = l$  (A1d)

937 **1. Input phase lattice constants**

938 These are the physical dimensions (a, b, c) of the unit cell in a crystal lattice. The number of unique  
 939 terms depends on crystal symmetry but three input values are required.

940 **2. Input rotation axis**

941 The five-parameter boundary orientation determination method requires the crystallographic

942 orientation of the rotation axis and boundary plane normal directions. The former is input here.

943 However, the value may involve calculations in Sections 4 and/or 5.

### 944 **3. Calculate normalised rotation axis**

945 The calculation of TTC involves the normalised rotation axis (e.g. Amouyal et al., 2005; Jhang et  
946 al., 2018). Normalisation,  $[\bar{u}\bar{v}\bar{w}]$  is achieved via,

$$947 \quad \bar{u} = u/\Sigma \quad \bar{v} = v/\Sigma \quad \bar{w} = w/\Sigma \quad (A2)$$

948 where  $\Sigma = (a \times u + b \times v + c \times w)^{1/2}$ .

### 949 **4. Calculate normal [uvw] to plane (hkl) - orthorhombic lattices**

950 In general, the normal direction to a crystal plane in non-cubic crystal lattices does not consist of the  
951 same indices due to the different lengths of the lattice constants, although there are symmetry-  
952 dependent exceptions. For example, in the orthorhombic olivine lattice, the normal to the plane  
953 (111) is not [111] but [413]. The main text explains how the reciprocal lattice concept can be used  
954 to solve this problem (i.e. Eqns 9 and 10).

### 955 **5. Calculate plane (hkl) from two directions $\langle u_1v_1w_1 \rangle$ , $\langle u_2v_2w_2 \rangle$ ,**

956 When using Spherical Kikuchi Maps, lattice planes are not always displayed, particularly as their  
957 indices increase. Fortunately, any plane can be determined from two known directions (i.e. zone  
958 axes) through which it passes. First, the two zone axes are written twice, one beneath the other:

$$959 \quad \begin{array}{cccccc} \mathbf{u}_1 & \mathbf{v}_1 & \mathbf{w}_1 & \mathbf{u}_1 & \mathbf{v}_1 & \mathbf{w}_1 \\ 960 \quad \mathbf{u}_2 & \mathbf{v}_2 & \mathbf{w}_2 & \mathbf{u}_2 & \mathbf{v}_2 & \mathbf{w}_2 \end{array}$$

961 Next, the first and last pairs are excluded. Finally, the lattice plane is calculated from,

$$962 \quad h = v_1 \times w_2 - v_2 \times w_1 \quad k = w_1 \times u_2 - u_1 \times w_2 \quad l = u_1 \times v_2 - v_1 \times u_2 \quad (A3)$$

### 963 **6. Calculate tilt/twist component (TTC)**

964 This is calculated simply from Eqn. 3 in the main text using the normalised rotation axis and  
965 boundary plane normal indices. The former is automatically copied into the calculation; the latter is  
966 input manually after appropriate use of sections 4 and/or 5.

Excel spreadsheet to assist calculation of five-parameter based orientation of intra/inte								
<b>Input values: BOLD RED; output values BOLD BLACK</b>								
<b>0. Miller/Miller-Bravais Conversions (hexagonal and trigonal lattices)</b>								
Miller-Bravais to Miller								
Direction	<U	V	T	W>	to	<u	v	w>
	<b>1</b>	<b>1</b>	<b>-2</b>	<b>0</b>		<b>3</b>	<b>3</b>	<b>0</b>
Plane	{H	K	L	}	to	{h	k	l}
	<b>1</b>	<b>1</b>	<b>-2</b>	<b>0</b>		<b>1</b>	<b>1</b>	<b>0</b>
Miller to Miller-Bravais								
Direction	<u	v	w>	to	<U	V	T	W>
	<b>3</b>	<b>3</b>	<b>0</b>		<b>1</b>	<b>1</b>	<b>-2</b>	<b>0</b>
Plane	{h	k	l}	to	{H	K	L	}
	<b>1</b>	<b>1</b>	<b>0</b>		<b>1</b>	<b>1</b>	<b>-2</b>	<b>0</b>
<b>1. Input Phase Lattice Constants - Olivine</b>								
	a	b	c					
	<b>4.756</b>	<b>10.21</b>	<b>5.98</b>					
<b>2. Input Rotation Axis</b>								
	u	v	w					
	<b>0</b>	<b>0</b>	<b>1</b>					
<b>3. Calculate Normalised Rotation Axis</b>								
Products of lattice constants and crystal direction								
	0.000	0.000	5.980					
SQRT of squares of products = 5.980								
Calculate normalised crystal direction:								
	0.000	0.000	1.000					
<b>4. Calculate normals [uvw] to planes (hkl) in orthorhombic lattices</b>								
Calculate reciprocal lattice except for [100], [010], [001] // $\perp$ (100), (010), (001)								
Lattice volume = 290.381								
a*	0.210	b*	0.098	c*	0.167			
Conversion								
u	=	a*.a*	0	0	•	h		
v	=	0	b*.b*	0	•	k		
w	=	0	0	c*.c*	•	l		
Input plane (hkl)								
	=	0.04421	0	0	•	<b>0</b>		
		0	0.009593	0	•	<b>0</b>		
		0	0	0.027964	•	<b>1</b>		
	=	0	0	0	=	<b>0</b>		
		0	x 100 =	0	=	<b>0</b>		
		0.027964		2.796389	=	<b>3</b>		
<b>5. Calculate plane (hkl) containing two directions &lt;uvw&gt;</b>								
Input first direction <u1, v1 w1>			Input second direction <u2, v2 w2>					
u1	v1	w1	u2	v2	w2			
<b>1</b>	<b>0</b>	<b>0</b>	<b>0</b>	<b>0</b>	<b>3</b>			
Conversion expression								
1	0	0	1	0	0			
0	0	3	0	0	3			
Calculate common plane								
h	k	l						
<b>0</b>	<b>-3</b>	<b>0</b>						
<b>6. Calculate tilt/twist component (tilt = 0 &lt; TTC &lt; 1 = twist)</b>								
Rotation axis (A <sub>[uvw]</sub> )				Grain boundary normal (B <sub>[uvw]</sub> )				
u	v	w	$\theta$	u	v	w	$\theta$	
0	0	1	0	<b>0</b>	<b>0</b>	<b>3</b>	<b>4.32</b>	
Products of lattice parameters and axis indices				Products of lattice parameters and axis indices				
u	v	w	$\theta$	u	v	w	$\theta$	
0.000	0.000	5.980	0.000	0.000	0.000	17.940	4.320	
SQRT of squares of indices = 5.980				SQRT of squares of indices = 17.940				
Calculate normalised rotation axis:				Calculate normalised grain boundary normal:				
A* <sub>[uvw]</sub> =	0.000	0.000	1.000	N* <sub>[uvw]</sub> =	0.000	0.000	1.000	
<b>TTC = A*<sub>[uvw]</sub> • N*<sub>[uvw]</sub> =</b>			<b>1.000</b>					